Fourier Series Expansion in a Non-Orthogonal System of Coordinates for the Simulation of 3D AC Borehole Resistivity Measurements

D. Pardo[a], C. Torres-Verdín[a], M. J. Nam[a],
M. Paszynski[b], and V. M. Calo[c]

[a] *Department of Petroleum and Geosystems Engineering, The University of Texas at Austin*

[b] *Department of Computer Science, AGH University of Technology, Krakow, Poland*

[c] *Institute for Computational Engineering and Sciences (ICES), The University of Texas at Austin*

Abstract

We describe a new method to simulate 3D resistivity borehole measurements acquired with alternate-current (AC) logging instruments. The method combines the use of a Fourier series expansion in a non-orthogonal system of coordinates with an existing 2D goal-oriented higher-order self-adaptive *hp*-Finite Element (FE) algorithm.

The new method is used to simulate measurements acquired with both wireline and logging-while-drilling (LWD) borehole logging instruments in deviated wells. It enables a considerable reduction of the computational complexity with respect to available 3D simulators, since the number of Fourier modes (basis functions) needed to solve practical applications is limited (typically, below 13). The fast convergence of the method is studied via numerical experimentation by simulating two wireline and one LWD instruments moving in a deviated well across a possibly invaded formation.

Numerical results confirm the efficiency and reliability of the method for simulating challenging 3D AC resistivity borehole problems in deviated wells, while avoiding the expensive construction of optimal 3D grids. Thus, we accurately simulate challenging electrodynamic problems employing only a few seconds (or minutes) of CPU time per logging position.

The method is especially well-suited for inversion of triaxial electromagnetic (EM) measurements, since we demonstrate that the number of Fourier modes needed for the exact representation of the material function is limited to only one (the central mode) for the case of borehole measurements acquired in deviated wells.

Key words: Fourier Series Expansion, Electromagnetism, *hp*-FE Method,

1 Introduction

Resistivity logging instruments have been used during the last eighty years to quantify the spatial distribution of electrical conductivity in the vicinity of boreholes. Conductivity of the rock formation is utilized to asses the material properties of the subsurface, and is routinely used by oil-companies to estimate the amount of hydrocarbons (oil and gas) existing within a reservoir.

A variety of logging instruments have been employed to estimate the electrical conductivity of rock formations. In this paper, we focus on EM devices operating at one or several particular frequencies. Almost all existing resistivity logging instruments operate at particular frequencies, and therefore, are governed by the time-harmonic Maxwell's equations.

To improve the interpretation of results obtained with EM logging instruments, and thus, to better quantify and determine the existing subsurface materials and increase hydrocarbon recovery, diverse methods have been developed to perform numerical simulations as well as to invert well-log measurements. In [1], we described a new numerical method based on a Fourier series expansion in a non-orthogonal system of coordinates combined with a 2D self-adaptive *hp* goal-oriented Finite Element (FE) method. This method was formulated and applied to direct-current (DC) resistivity problems, and it enabled fast and accurate simulations of previously unsolved EM simulation problems in deviated wells.

In this paper, we extend the numerical method presented in [1] to alternate current (AC) resistivity logging instruments, which operate at non-zero frequencies. The proposed method entails the use of a change of variables and a Fourier-Finite Element Method [2,3]. In addition, we illustrate the convergence properties of our method when applied to challenging borehole logging problems. The extension of the method described in [1] to 3D AC problems is non-trivial, and it involves the following challenges:

- Derivation of time-harmonic variational formulation of Maxwell's equations in an arbitrary system of coordinates.
- Implementation of mixed variational formulations involving simultaneously the use of $H(\mathbf{curl})$ and H^1 FE discretizations.
- Development of a parallel implementation and fast direct solvers to reduce the CPU time and meet the increased memory requirements needed by simulations of challenging AC logging measurements.

We emphasize that while DC simulations utilize a single scalar-valued variable (the scalar potential), AC simulations require the use of three vector-valued variables, corresponding to three components of the EM fields. In addition, the final variational formulation we obtain for AC problems with our new method is neither Hermitian nor complex-symmetric [1]. As a result, the computational cost associated with simulations of AC measurements increases by approximately one order of magnitude with respect to that associated with simulations of DC measurements.

Other numerical methods developed within the oil industry for simulations of AC resistivity logging instruments include fast 1D and 2D axial-symmetric simulators such as, for example, those described in [4–7]. These simulators are unable to solve problems involving deviated wells [2], due to the dimensionality reduction. By contrast, 3D algorithms such as those described in [8–16] are capable of simulating resistivity measurements acquired in deviated wells. However, existing 3D simulators are not widely used by the logging industry in everyday logging-operations, either because the accuracy of these methods is compromised and/or the CPU time required for simulations exceeds reasonable limits (several hours per logging position).

The method described in this paper provides highly accurate and reliable results within reasonable CPU times, since it enables a significant reduction of the computational complexity with respect to conventional 3D simulators without a sacrifice in accuracy. In addition, the method is suitable for inverse problems, as well as for multi-physic applications. Therefore, it aims to become a widely used simulation strategy for problems arising in the logging industry.

The remainder of this paper is organized as follows: In Section 2 we introduce Maxwell's equations with appropriate boundary conditions. Then, we describe our method for AC problems and we provide a formal derivation of our final variational formulation. Implementation details of the method are described in Section 3. Numerical results included in Section 4 are focused toward validating the method and studying its applicability to everyday logging-operations. Finally, the main conclusions of this paper are summarized in Section 5.

2 Method

In this Section, we first introduce Maxwell's equations and we discuss the appropriate boundary conditions. Second, we derive a variational formulation for

[1] For DC problems, we obtain a Hermitian variational formulation, see [1].

[2] Nowadays, most wells are deviated, since they may extend over longer distances within the hydrocarbon layers, thereby enhancing hydrocarbon recovery.

3D time-harmonic Maxwell's equations in an arbitrary system of coordinates $(\zeta_1, \zeta_2, \zeta_3)$. Third, we assume that the solution in one of the directions in the new coordinate system, *e.g.* ζ_2, is periodic (for example, with period $[0,2\pi]$). Under this assumption, we employ a Fourier series expansion in terms of ζ_2 to derive the corresponding variational formulation in terms of the Fourier modal coefficients. Then, we consider the following non-orthogonal system of coordinates described in [1] (see also Fig. 1) for deviated wells in a borehole environment:

$$\begin{cases} x_1 = \zeta_1 \cos\zeta_2 \\ x_2 = \zeta_1 \sin\zeta_2 \\ x_3 = \zeta_3 + \theta_0 f(\zeta_1)\cos\zeta_2 \end{cases} \quad ; \quad f(\zeta_1) = \begin{cases} 0 & \zeta_1 < \rho_1 \\ \dfrac{\zeta_1 - \rho_1}{\rho_2 - \rho_1}\rho_2 & \rho_1 \le \zeta_1 \le \rho_2 \\ \zeta_1 & \zeta_1 > \rho_2 \end{cases} , \quad (1)$$

where $\theta_0 = \tan\theta$, θ is the dip angle [3], and ρ_1, ρ_2 are given values that depend upon each specific simulation problem.

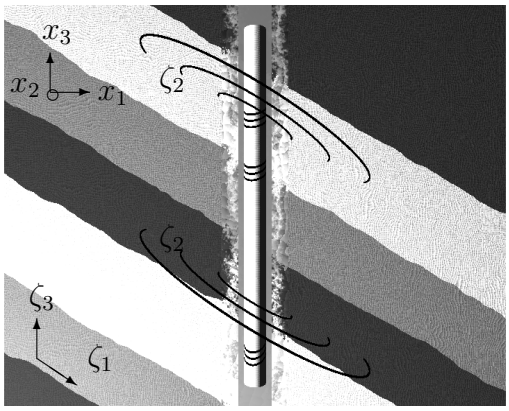

Fig. 1. Cross section showing the 3D geometry of a resistivity logging instrument in a vertical well penetrating dipping layers. Oblique circles indicate the "quasi-azimuthal" direction ζ_2 in the non-orthogonal system of coordinates $(\zeta_1, \zeta_2, \zeta_3)$.

The above coordinate system verifies the assumption stated above (*i.e.* the solution is periodic with respect to variable ζ_2, with period length equal to 2π) and, furthermore, requires only a few Fourier modes to represent exactly the change of coordinates and the material coefficients. Finally, we briefly describe the method employed for solving the resulting formulation via a 2D self-adaptive goal-oriented *hp*-FE method with variable order H^1- and $H(\mathbf{curl})$-discretizations.

Throughout the derivation presented in this section, we consider various formulations for time-harmonic Maxwell's equations. Specifically, we provide ex-

[3] The dip angle is the angle between the well trajectory and a normal vector to the layer boundaries.

tensive details for the so-called E-formulation (in terms of the electric field). We also describe the H-formulation (in terms of the magnetic field), and we sketch the major differences necessary to derive various vector-potential and stabilized formulations.

2.1 Time-Harmonic Maxwell's Equations

Assuming a time-harmonic dependence of the form $e^{j\omega t}$, with ω denoting angular frequency, Maxwell's equations in linear media can be written as

$$\begin{cases} \boldsymbol{\nabla} \times \mathbf{H} &= (\boldsymbol{\sigma} + j\omega\boldsymbol{\epsilon})\mathbf{E} + \mathbf{J}^{imp} & \text{Ampere's Law,} \\ \boldsymbol{\nabla} \times \mathbf{E} &= -j\omega\boldsymbol{\mu}\,\mathbf{H} - \mathbf{M}^{imp} & \text{Faraday's Law,} \\ \boldsymbol{\nabla} \cdot (\boldsymbol{\epsilon}\mathbf{E}) &= \rho & \text{Gauss' Law of Electricity, and} \\ \boldsymbol{\nabla} \cdot (\boldsymbol{\mu}\mathbf{H}) &= 0 & \text{Gauss' Law of Magnetism.} \end{cases} \tag{2}$$

In the above equations, $\mathbf{H}$ and $\mathbf{E}$ denote the magnetic and electric fields, respectively, tensors $\boldsymbol{\epsilon}, \boldsymbol{\mu}$, and $\boldsymbol{\sigma}$ stand for dielectric permittivity, magnetic permeability, and electrical conductivity of the media, respectively, ρ denotes the electric charge distribution, and $\mathbf{J}^{imp}, \mathbf{M}^{imp}$ are representations for the prescribed, impressed electric and magnetic current sources, respectively. We assume that $det(\boldsymbol{\mu}) \neq 0$, and $det(\boldsymbol{\sigma} + j\omega\boldsymbol{\epsilon}) \neq 0$.

By taking the divergence of Faraday's law, and applying Gauss' Law of magnetism, we find that $\mathbf{M}^{imp}$ is divergence free. We also emphasize that, as explained in [17], impressed currents are only mathematical symbols utilized to represent sources. However, we note it may be impossible to realize arbitrary sources in practice. In particular, $\mathbf{M}^{imp} = 0$ at zero-frequency is non-physical, since $\mathbf{M}^{imp}$ is always proportional to the frequency of operation.

2.1.1 Boundary Conditions (BCs)

There exist a variety of BCs that can be incorporated into Maxwell's equations. In the following, we describe those BCs that are of interest to the borehole logging applications discussed in this paper.

2.1.1.1 Perfect Electric Conductor (PEC). A PEC is an idealization of a highly conductive medium, that is, $\boldsymbol{\sigma} \to \infty$. The corresponding electric field $\mathbf{E}$ converges to zero by applying Ampere's law since, due to physical

considerations, we assume that $\boldsymbol{\sigma}\mathbf{E}$, $\boldsymbol{\epsilon}\mathbf{E}$, $\mathbf{J}^{imp} \in \boldsymbol{L}^2(\Omega)$. In the absence of impressed magnetic surface currents, Faraday's law implies that the tangential component of $\mathbf{E}$ and the normal component of $\boldsymbol{\mu}\mathbf{H}$ must remain continuous across material interfaces. Consequently, the tangential component of the electric field and the normal component of the magnetic field must vanish along the PEC boundary, *i.e.*,

$$\boldsymbol{n}\times\mathbf{E} = \mathbf{0} \quad ; \quad \boldsymbol{n}\cdot\mathbf{H} = \mathbf{0}\,, \tag{3}$$

where $\boldsymbol{n}$ is the unit normal (outward) vector. The tangential component of the magnetic field (surface current) and the normal component of the electric field (surface charge density) need not to be zero, and may be determined a-posteriori.

2.1.1.2 Source Antennas. Antennas are modeled by prescribing an impressed volume current $\mathbf{J}^{imp}$ or $\mathbf{M}^{imp}$. Using the equivalence principle (see, for example, [17]), one can replace the original impressed volume currents with the following equivalent surface currents (see [18] for details):

$$\mathbf{J}_S^{imp} = [\mathbf{n}\times\mathbf{H}]_S \quad ; \quad \mathbf{M}_S^{imp} = -[\mathbf{n}\times\mathbf{E}]_{\mathbf{S}}\,, \tag{4}$$

defined on an arbitrary surface S enclosing the support of the impressed volume currents, where $[\mathbf{n}\times\mathbf{H}]_S$ denotes the jump of $\mathbf{n}\times\mathbf{H}$ across S in the case of an interface condition, or simply $\mathbf{n}\times\mathbf{H}$ on S in the case of a boundary condition.

According to the BCs discussed above, we divide boundary $\Gamma = \partial\Omega$ as the disjoint union of

- Γ_E, where $\mathbf{M}_{\Gamma_E}^{imp} = -[\mathbf{n}\times\mathbf{E}]_{\Gamma_E}$ (with $\mathbf{M}_{\Gamma_E}^{imp}$ possibly zero), with
- Γ_H, where $\mathbf{J}_{\Gamma_H}^{imp} = [\mathbf{n}\times\mathbf{H}]_{\Gamma_H}$, (with $\mathbf{J}_{\Gamma_H}^{imp}$ possibly zero).

2.1.1.3 Closure of the Domain. A variety of BCs can be imposed on the boundary $\partial\Omega$ of a computational domain Ω such that the difference between solution of such a problem and solution of the original problem defined over $\mathbb{R}^3$ is small. For example, it is possible to use an infinite element technique [19], a Perfectly Matched Layer (PML) [20], a boundary element technique [21] or an absorbing BC. However, it is customary in geophysical logging applications to impose a homogeneous Dirichlet BC on the boundary of a sufficiently large computational domain, since the EM fields decay exponentially in the presence of lossy media. For simplicity, in the simulations presented in the paper we will follow the Dirichlet BC approach.

2.2 E-Formulation

In this subsection, we describe our method in terms of the unknown electric field $\mathbf{E}$. First, we derive a variational formulation in Cartesian coordinates $\mathbf{x} = (x_1, x_2, x_3)$. Then, we introduce a (possibly non-orthogonal) system of coordinates $\boldsymbol{\zeta} = (\zeta_1, \zeta_2, \zeta_3)$, and we derive the corresponding variational formulation. Finally, we assume that one of the directions in the new coordinate system, *e.g.* ζ_2, is defined in a bounded domain (for example, [0,2π)). Under this assumption, we construct a Fourier series expansion in terms of ζ_2 to derive the corresponding variational formulation in terms of the Fourier modal coefficients.

2.2.1 3D Variational Formulation in Cartesian Coordinates

First, we define the L^2-inner product of two (possibly complex- and vector-valued) functions f and g as:

$$\langle f, g \rangle_{L^2(\Omega)} = \int_{\Omega} f^* g dV \ , \tag{5}$$

where f^* denotes the adjoint (conjugate transpose) of function f.

By multiplying the inverse of magnetic permeability tensor $\boldsymbol{\mu}$ by Faraday's law, pre-multiplying the resulting equation by $\boldsymbol{\nabla}\times\mathbf{F}$, where $\mathbf{F} \in H_{\Gamma_E}(\mathbf{curl};\Omega) = \{\mathbf{F} \in H(\mathbf{curl};\Omega) \ : (\mathbf{n}\times\mathbf{F})|_{\Gamma_E} = 0 \}$ is an arbitrary test function, integrating over domain $\Omega \subset \mathbb{R}^3$ by parts, and applying Ampere's law, we arrive at the following variational formulation after incorporating the natural and essential boundary conditions over $\Gamma_H \subset \partial\Omega$ and $\Gamma_E \subset \partial\Omega$, respectively:

$$\begin{cases} \text{Find } \mathbf{E} \in \mathbf{E}_{\Gamma_E} + H_{\Gamma_E}(\mathbf{curl};\Omega) \text{ such that:} \\ \left\langle \boldsymbol{\nabla}\times\mathbf{F} \ , \ \boldsymbol{\mu}^{-1}\boldsymbol{\nabla}\times\mathbf{E}) \right\rangle_{L^2(\Omega)} - \left\langle \mathbf{F} \ , \ \boldsymbol{k}^2\mathbf{E} \right\rangle_{L^2(\Omega)} \\ = -j\omega \left\langle \mathbf{F} \ , \ \mathbf{J}^{imp} \right\rangle_{L^2(\Omega)} \ + j\omega \left\langle \mathbf{F}_t \ , \ \mathbf{J}_S^{imp} \right\rangle_{L^2(\Gamma_H)} \\ - \left\langle \boldsymbol{\nabla}\times\mathbf{F} \ , \ \boldsymbol{\mu}^{-1}\mathbf{M}^{imp} \right\rangle_{L^2(\Omega)} \quad \forall\, \mathbf{F} \in H_{\Gamma_E}(\mathbf{curl};\Omega) \ , \end{cases} \tag{6}$$

where $\boldsymbol{k}^2 = \omega^2\boldsymbol{\epsilon} - j\omega\boldsymbol{\sigma}$ is the wave number, $\mathbf{E}_{\Gamma_E}$ is a lift (typically $\mathbf{E}_{\Gamma_E} = 0$) of the essential boundary condition data $\mathbf{E}_{\Gamma_E} = -\mathbf{M}^{imp}_{\Gamma_E}$ (denoted with the same symbol), $\mathbf{F}_t = \mathbf{F} - (\mathbf{F}\cdot\mathbf{n})\cdot\mathbf{n}$ is the tangential component of vector $\mathbf{F}$ on Γ_H, and $\mathbf{n}$ is the unit normal outward (with respect to Ω) vector.

2.2.2 3D Variational Formulation in an Arbitrary System of Coordinates

Let $\mathbf{x} = (x_1, x_2, x_3)$ designate the Cartesian system of coordinates. We introduce an arbitrary (possibly non-orthogonal) system of coordinates $\boldsymbol{\zeta} = (\zeta_1, \zeta_2, \zeta_3)$, with $\boldsymbol{\mathcal{J}}$ and $|\boldsymbol{\mathcal{J}}|$ identifying the Jacobian matrix and determinant of the change of variables, respectively. Our change of coordinates is described by mapping $\mathbf{x} = \boldsymbol{\psi}(\boldsymbol{\zeta})$, which is assumed to be bijective, with positive Jacobian determinant, and globally continuous (see [22], Chapter XII).

Given an arbitrary vector-valued function $\mathbf{E} = \mathbf{E}(\mathbf{x})$, we denote $\hat{\mathbf{E}} := \mathbf{E} \circ \boldsymbol{\psi} = \hat{\mathbf{E}}(\boldsymbol{\zeta})$. Let $\mathbf{e}_{x_i}$ and $\mathbf{e}_{\zeta_i}$ be the basis vectors corresponding to the Cartesian and new systems of coordinates, respectively. Using Einstein summation convention, we have $\mathbf{E} = E_{x_i}\mathbf{e}_{x_i}$, $\hat{\mathbf{E}} = \tilde{E}_{\zeta_i}\mathbf{e}_{\zeta_i}$, where according to the chain rule:

$$E_{x_i} = \tilde{E}_{\zeta_l}\frac{\partial \zeta_l}{\partial x_i} \,. \tag{7}$$

We define vector $\tilde{\mathbf{E}} := \tilde{E}_{\zeta_i}\mathbf{e}_{x_i}$ (similarly, we also define $\tilde{\mathbf{F}} := \tilde{F}_{\zeta_i}\mathbf{e}_{x_i}$, $\tilde{\mathbf{J}}^{imp} := \tilde{J}^{imp}_{\zeta_i}\mathbf{e}_{x_i}$, $\tilde{\mathbf{M}}^{imp} := \tilde{M}^{imp}_{\zeta_i}\mathbf{e}_{x_i}$). Then:

$$\begin{aligned}
&\mathbf{E} = E_{x_i}\mathbf{e}_{x_i} = \tilde{E}_{\zeta_l}\frac{\partial \zeta_l}{\partial x_i}\mathbf{e}_{x_i} = \boldsymbol{\mathcal{J}}^{-1^*}\tilde{\mathbf{E}} \\
&\boldsymbol{\nabla}\times\mathbf{E} = \boldsymbol{\epsilon}_{ijk}\frac{\partial E_k}{\partial x_j}\mathbf{e}_{x_i} = \frac{1}{|\boldsymbol{\mathcal{J}}|}\frac{\partial x_i}{\partial \zeta_n}\left(\boldsymbol{\epsilon}_{nml}\frac{\partial \tilde{E}_{\zeta_l}}{\partial \zeta_m}\right)\mathbf{e}_{x_i} = \frac{\boldsymbol{\mathcal{J}}}{|\boldsymbol{\mathcal{J}}|}\boldsymbol{\nabla}^{\boldsymbol{\zeta}}\times\tilde{\mathbf{E}} \,,
\end{aligned} \tag{8}$$

where $\boldsymbol{\epsilon}_{ijk}$ is the so-called *Levi-Civita* symbol, defined as 0 if $i = j$, $i = k$, or $j = k$, as 1 if ijk is an even permutation of 123, and as -1 if ijk is an odd permutation of 123. We define $\boldsymbol{\nabla}^{\boldsymbol{\zeta}}\times\tilde{\mathbf{E}} = (\nabla^{\zeta_n} \times \tilde{\mathbf{E}})\ \mathbf{e}_{x_n}$, where $\nabla^{\zeta_n} \times \tilde{\mathbf{E}}$ is equal to

$$\nabla^{\zeta_n} \times \tilde{\mathbf{E}} := \boldsymbol{\epsilon}_{nml}\frac{\partial \tilde{E}_{\zeta_l}}{\partial \zeta_m} \,. \tag{9}$$

Therefore,

$$\begin{aligned}
\left\langle \boldsymbol{\nabla}\times\mathbf{F} \,,\, \boldsymbol{\mu}^{-1}\boldsymbol{\nabla}\times\mathbf{E} \right\rangle_{L^2(\Omega)} &= \left\langle \frac{\boldsymbol{\mathcal{J}}}{|\boldsymbol{\mathcal{J}}|}\boldsymbol{\nabla}^{\boldsymbol{\zeta}}\times\tilde{\mathbf{F}} \,,\, \tilde{\boldsymbol{\mu}}^{-1}\frac{\boldsymbol{\mathcal{J}}}{|\boldsymbol{\mathcal{J}}|}\boldsymbol{\nabla}^{\boldsymbol{\zeta}}\times\tilde{\mathbf{E}} \right\rangle_{L^2(\Omega)} \\
&= \left\langle \boldsymbol{\nabla}^{\boldsymbol{\zeta}}\times\tilde{\mathbf{F}} \,,\, \left(|\boldsymbol{\mathcal{J}}|\boldsymbol{\mathcal{J}}^{-1}\tilde{\boldsymbol{\mu}}(|\boldsymbol{\mathcal{J}}|\boldsymbol{\mathcal{J}}^{-1})^*\right)^{-1}\boldsymbol{\nabla}^{\boldsymbol{\zeta}}\times\tilde{\mathbf{E}} \right\rangle_{L^2(\Omega)} \,,
\end{aligned} \tag{10}$$

where $\tilde{\boldsymbol{\mu}} = \boldsymbol{\mu} \circ \boldsymbol{\psi}$. For the derivation of the above equality, we have used the

relationship $\boldsymbol{\mathcal{J}}^{*}\tilde{\boldsymbol{\mu}}^{-1}\boldsymbol{\mathcal{J}} = \left(\boldsymbol{\mathcal{J}}^{-1}\tilde{\boldsymbol{\mu}}\boldsymbol{\mathcal{J}}^{*^{-1}}\right)^{-1} = \left(\boldsymbol{\mathcal{J}}^{-1}\tilde{\boldsymbol{\mu}}\boldsymbol{\mathcal{J}}^{-1^{*}}\right)^{-1}$. We also obtain:

$$
\begin{aligned}
\left\langle \mathbf{F}\ ,\ \boldsymbol{k}^2\mathbf{E}\right\rangle_{L^2(\Omega)} &= \left\langle \tilde{\mathbf{F}}\ ,\ \boldsymbol{\mathcal{J}}^{-1}\tilde{\boldsymbol{k}}^2\boldsymbol{\mathcal{J}}^{-1^{*}}\tilde{\mathbf{E}}\right\rangle_{L^2(\Omega)}\ , \\
\left\langle \mathbf{F}\ ,\ \mathbf{J}^{imp}\right\rangle_{L^2(\Omega)} &= \left\langle \tilde{\mathbf{F}}\ ,\ \boldsymbol{\mathcal{J}}^{-1}\boldsymbol{\mathcal{J}}^{-1^{*}}\tilde{\mathbf{J}}^{imp}\right\rangle_{L^2(\Omega)}\ , \\
\left\langle \boldsymbol{\nabla}\times\mathbf{F}\ ,\ \boldsymbol{\mu}^{-1}\mathbf{M}^{imp}\right\rangle_{L^2(\Omega)} &= \left\langle \boldsymbol{\nabla}^{\boldsymbol{\zeta}}\times\tilde{\mathbf{F}}\ ,\ \left(\frac{\boldsymbol{\mathcal{J}}}{|\boldsymbol{\mathcal{J}}|}\right)^{*}\tilde{\boldsymbol{\mu}}^{-1}\boldsymbol{\mathcal{J}}^{-1^{*}}\tilde{\mathbf{M}}^{imp}\right\rangle_{L^2(\Omega)}\ , \text{and} \\
\left\langle \mathbf{F}_t\ ,\ \mathbf{J}_S^{imp}\right\rangle_{L^2(\Gamma_H)} &= \left\langle \tilde{\mathbf{F}}_t\ ,\ \boldsymbol{\mathcal{J}}^{-1}\boldsymbol{\mathcal{J}}^{-1^{*}}\tilde{\mathbf{J}}_S^{imp}\right\rangle_{L^2(\tilde{\Gamma}_H)}\ .
\end{aligned}
\tag{11}
$$

Following the ideas discussed in [23] of including the metric-dependent variables within the material coefficients, we define the following new tensors and functions:

$$
\begin{aligned}
&\tilde{\boldsymbol{\sigma}}_{NEW} := \boldsymbol{\mathcal{J}}^{-1}\tilde{\boldsymbol{\sigma}}\boldsymbol{\mathcal{J}}^{-1^{*}}|\boldsymbol{\mathcal{J}}| \quad ; \quad \tilde{\boldsymbol{\epsilon}}_{NEW} := \boldsymbol{\mathcal{J}}^{-1}\tilde{\boldsymbol{\epsilon}}\boldsymbol{\mathcal{J}}^{-1^{*}}|\boldsymbol{\mathcal{J}}|\ , \\
&\tilde{\boldsymbol{\mu}}_{NEW} := \boldsymbol{\mathcal{J}}^{-1}\tilde{\boldsymbol{\mu}}\boldsymbol{\mathcal{J}}^{-1^{*}}|\boldsymbol{\mathcal{J}}| \quad ; \quad \tilde{\boldsymbol{k}}^2_{NEW} := \boldsymbol{\mathcal{J}}^{-1}\tilde{\boldsymbol{k}}^2\boldsymbol{\mathcal{J}}^{-1^{*}}|\boldsymbol{\mathcal{J}}|\ , \\
&\tilde{\mathbf{J}}^{imp}_{NEW} := \boldsymbol{\mathcal{J}}^{-1}\boldsymbol{\mathcal{J}}^{-1^{*}}|\boldsymbol{\mathcal{J}}|\tilde{\mathbf{J}}^{imp} \quad ; \quad \tilde{\mathbf{M}}^{imp}_{NEW} := \boldsymbol{\mathcal{J}}^{-1}\boldsymbol{\mathcal{J}}^{-1^{*}}|\boldsymbol{\mathcal{J}}|\tilde{\mathbf{M}}^{imp}\ , \\
&\tilde{\mathbf{J}}^{imp}_{S,NEW} := \boldsymbol{\mathcal{J}}^{-1}\boldsymbol{\mathcal{J}}^{-1^{*}}|\boldsymbol{\mathcal{J}}_S|\tilde{\mathbf{J}}^{imp}_S \quad ; \quad \tilde{\mathbf{M}}^{imp}_{S,NEW} := \boldsymbol{\mathcal{J}}^{-1}\boldsymbol{\mathcal{J}}^{-1^{*}}|\boldsymbol{\mathcal{J}}_S|\tilde{\mathbf{M}}^{imp}_S\ ,
\end{aligned}
\tag{12}
$$

where $|\boldsymbol{\mathcal{J}}_S|$ is the Jacobian determinant associated with the change of variables restricted to the two-dimensional surface Γ_H.

REMARK: The new material coefficients and load data introduced above are consistent with those corresponding to the DC case (see [1]), since $\tilde{\boldsymbol{\sigma}}_{NEW}$ is identical for both DC and AC regimes, and

$$
\begin{aligned}
\tilde{f}_{NEW} := \boldsymbol{\nabla}\cdot\tilde{\mathbf{J}}^{imp}_{NEW} = \boldsymbol{\nabla}\cdot\tilde{\mathbf{J}}^{imp}\boldsymbol{\mathcal{G}}^{nm}|\boldsymbol{\mathcal{J}}| = \boldsymbol{\mathcal{G}}_{nm}\frac{\partial\tilde{\boldsymbol{\mathcal{J}}}_{\zeta_k}}{\partial\zeta_k}\boldsymbol{\mathcal{G}}^{nm}|\boldsymbol{\mathcal{J}}| = \\
\frac{\partial\tilde{\boldsymbol{\mathcal{J}}}_{\zeta_k}}{\partial\zeta_k}|\boldsymbol{\mathcal{J}}| = \tilde{f}|\boldsymbol{\mathcal{J}}|\ ,
\end{aligned}
\tag{13}
$$

where $\boldsymbol{\mathcal{G}} = \boldsymbol{\mathcal{G}}_{nm} = \boldsymbol{\mathcal{J}}^{*}\boldsymbol{\mathcal{J}}$ is the metric tensor and $\boldsymbol{\mathcal{G}}^{-1} = \boldsymbol{\mathcal{G}}^{nm}$ its inverse.

Our new space of *admissible solutions* is given by $\tilde{V}(\Omega) = \tilde{H}_{\Gamma_E}(\mathbf{curl};\Omega) = \{\tilde{\mathbf{F}}\ :\ (\mathbf{n}\times\tilde{\mathbf{F}})|_{\Gamma_E} = 0\ ,\ \boldsymbol{\mathcal{J}}^{-1^{*}}\tilde{\mathbf{F}} \in \boldsymbol{L}^2(\Omega)\ ,\ \dfrac{\boldsymbol{\mathcal{J}}}{|\boldsymbol{\mathcal{J}}|}\boldsymbol{\nabla}^{\boldsymbol{\zeta}}\times\tilde{\mathbf{F}} \in \boldsymbol{L}^2(\Omega)\}$. See Section 3.1 for details about suitable discretizations of this $H(\mathbf{curl})$-type space.

By dropping the $\tilde{}$ symbol from the notation, we arrive at our original variational formulation (6) in terms of our new coordinate system, with new ma-

terial and load data, namely,

$$\begin{cases} \text{Find } \mathbf{E} \in \mathbf{E}_{\Gamma_E} + V(\Omega) \text{ such that:} \\ \left\langle \boldsymbol{\nabla}^{\boldsymbol{\zeta}} \times \mathbf{F} \, , \, \boldsymbol{\mu}_{NEW}^{-1} \, \boldsymbol{\nabla}^{\boldsymbol{\zeta}} \times \mathbf{E} \right\rangle_{\mathcal{L}^2(\Omega)} - \left\langle \mathbf{F} \, , \, \boldsymbol{k}_{NEW}^2 \mathbf{E} \right\rangle_{\mathcal{L}^2(\Omega)} = \\ -j\omega \left\langle \mathbf{F} \, , \, \mathbf{J}_{NEW}^{imp} \right\rangle_{\mathcal{L}^2(\Omega)} + j\omega \left\langle \mathbf{F}_t \, , \, \mathbf{J}_{S,NEW}^{imp} \right\rangle_{\mathcal{L}^2(\Gamma_H)} \\ - \left\langle \boldsymbol{\nabla}^{\boldsymbol{\zeta}} \times \mathbf{F} \, , \, \boldsymbol{\mu}_{NEW}^{-1} \mathbf{M}_{NEW}^{imp} \right\rangle_{\mathcal{L}^2(\Omega)} \; \forall \, \mathbf{F} \in V(\Omega) \, , \end{cases} \tag{14}$$

where our $\mathcal{L}^2$ inner-product definition *does not* include the Jacobian determinant $|\boldsymbol{\mathcal{J}}|$ corresponding to the change of variables, since information about the Jacobian determinant $|\boldsymbol{\mathcal{J}}|$ is already included in both the new material coefficients and load data. Thus, for arbitrary functions f and g defined on the $\boldsymbol{\zeta}$-coordinate system, our inner-product is defined as

$$\langle f, g \rangle_{\mathcal{L}^2(\Omega)} = \int\limits_{\Omega(\zeta_1,\zeta_2,\zeta_3)} f^* g \, d\zeta_1 d\zeta_2 d\zeta_3 \, . \tag{15}$$

REMARK: The Jacobian matrix associated with the change of coordinates defined in Equation (1) is real-valued. However, we have used the notation $\boldsymbol{\mathcal{J}}^*$ rather than $\boldsymbol{\mathcal{J}}^T$ to account for possibly complex-valued Jacobian matrices, as those arising when considering PMLs [24,25,20].

2.2.3 Fourier Series Expansion

Let ζ_2 (a variable in the new coordinate system) be defined in a bounded domain, for example, $[0, 2\pi)$. Then, any function $\mathbf{G}$ in the new coordinate system is periodic (with period length equal to 2π) and, therefore, can be expressed in terms of its Fourier series expansion, namely,

$$\mathbf{G} = \sum_{l=-\infty}^{l=\infty} \mathbf{G}_l e^{jl\zeta_2} = \sum_{l=-\infty}^{l=\infty} \mathcal{F}_l(\mathbf{G}) e^{jl\zeta_2} \, , \tag{16}$$

where $e^{jl\zeta_2}$ are the modes, and $\mathcal{F}_l(\mathbf{G}) = \mathbf{G}_l$ are the modal coefficients, which are independent of variable ζ_2. Notice that symbol $\mathcal{F}_l$, when applied to a vector-valued function $\mathbf{G} = (G_1, G_2, G_3)$, produces a vector (or matrix) of the same dimensions, with each of the components being equal to the l-th Fourier modal coefficient corresponding to the component of the original vector (or matrix). For example,

$$\mathcal{F}_l(G_1 \quad G_2 \quad G_3) = (\mathcal{F}_l G_1 \quad \mathcal{F}_l G_2 \quad \mathcal{F}_l G_3) = (G_{1,l} \quad G_{2,l} \quad G_{3,l}) \, . \tag{17}$$

We have the following properties:

$$\begin{aligned}
&\frac{\partial(\mathcal{F}_l(\mathbf{G})e^{jl\zeta_2})}{\partial\zeta_1} = \mathcal{F}_l\left(\frac{\partial\mathbf{G}}{\partial\zeta_1}\right)\, e^{jl\zeta_2}\,,\\
&\frac{\partial(\mathcal{F}_l(\mathbf{G})e^{jl\zeta_2})}{\partial\zeta_2} = jl\mathcal{F}_l(\mathbf{G})\, e^{jl\zeta_2}\,,\\
&\frac{\partial(\mathcal{F}_l(\mathbf{G})e^{jl\zeta_2})}{\partial\zeta_3} = \mathcal{F}_l\left(\frac{\partial\mathbf{G}}{\partial\zeta_3}\right)\, e^{jl\zeta_2}\,.
\end{aligned} \tag{18}$$

Furthermore, by invoking the Fourier series expansion of $\mathbf{G}$, we obtain

$$\mathcal{F}_l\left(\frac{\partial\mathbf{G}}{\partial\zeta_2}\right) := \mathcal{F}_l\left(\frac{\partial(\sum_k \mathbf{G}_k e^{jk\zeta_2})}{\partial\zeta_2}\right) = \mathcal{F}_l\left(\sum_k jk\mathbf{G}_k e^{jk\zeta_2}\right) = jl\mathcal{F}_l(\mathbf{G})\,. \tag{19}$$

Finally, from property (19) and definition of $\boldsymbol{\nabla^{\zeta}}\times\mathbf{G}$, we conclude that

$$\mathcal{F}_l(\boldsymbol{\nabla^{\zeta}}\times\mathbf{G}) = \left[\boldsymbol{\nabla^{\zeta}}\times(F_l(\mathbf{G})e^{jl\zeta_2})\right] e^{-jl\zeta_2}. \tag{20}$$

By employing the Fourier series expansion representation for $\mathbf{E}$, $\mathbf{E}_D$, $\boldsymbol{k}^2_{NEW}$, $\boldsymbol{\mu}^{-1}_{NEW}$, $\mathbf{J}^{imp}_{NEW}$, $\mathbf{M}^{imp}_{NEW}$, and $\mathbf{J}_{S,NEW}$, variational formulation (14) can be expressed as:

$$\begin{cases}
\text{Find } \mathcal{F}_l(\mathbf{E})e^{jl\zeta_2} \in \mathcal{F}_l(\mathbf{E}_{\Gamma_E})e^{jl\zeta_2} + V(\Omega) \text{ such that:}\\
\left\langle \boldsymbol{\nabla^{\zeta}}\times\mathbf{F}\,,\, \mathcal{F}_p(\boldsymbol{\mu}^{-1}_{NEW})\, \mathcal{F}_l(\boldsymbol{\nabla^{\zeta}}\times\mathbf{E})e^{j(l+p)\zeta_2}\right\rangle_{\mathcal{L}^2(\Omega)}\\
\quad -\left\langle \mathbf{F}\,,\, \mathcal{F}_p(\boldsymbol{k}^2_{NEW})\mathcal{F}_l(\mathbf{E})e^{j(l+p)\zeta_2}\right\rangle_{\mathcal{L}^2(\Omega)}\\
\quad = -j\omega\left\langle \mathbf{F}\,,\, \mathcal{F}_l(\mathbf{J}^{imp}_{NEW})e^{jl\zeta_2}\right\rangle_{\mathcal{L}^2(\Omega)}\\
\quad +j\omega\left\langle \mathbf{F}_t\,,\, \mathcal{F}_l(\mathbf{J}^{imp}_{S,NEW})e^{jl\zeta_2}\right\rangle_{\mathcal{L}^2(\Gamma_H)}\\
\quad -\left\langle \boldsymbol{\nabla^{\zeta}}\times\mathbf{F}\,,\, \mathcal{F}_p(\boldsymbol{\mu}^{-1}_{NEW})\mathcal{F}_l(\mathbf{M}^{imp}_{NEW})e^{j(l+p)\zeta_2}\right\rangle_{\mathcal{L}^2(\Omega)}\\
\quad \forall\, \mathbf{F} \in V(\Omega)\,.
\end{cases} \tag{21}$$

To derive the above formula, we have utilized equation (20). We note that we are employing Einstein summation convention, with $-\infty \leq l, p \leq \infty$, and we are assuming that Γ_E and Γ_H are independent of ζ_2.

For a mono-modal test function $\mathbf{F} = \mathcal{F}_k(\mathbf{F})e^{jk\zeta_2}$, variational problem (21) reduces by orthogonality of the Fourier modes in L^2 to

$$\begin{cases} \text{Find } \mathcal{F}_k(\mathbf{E}) \in \mathcal{F}_k(\mathbf{E}_{\Gamma_E(\Omega_{2D})}) + \mathcal{V}_k(\Omega) \text{ such that:} \\ \left\langle \mathcal{F}_k(\boldsymbol{\nabla}^{\boldsymbol{\zeta}}\times\mathbf{F}) \, , \, \mathcal{F}_{k-l}(\boldsymbol{\mu}_{NEW}^{-1}) \, \mathcal{F}_l(\boldsymbol{\nabla}^{\boldsymbol{\zeta}}\times\mathbf{E}) \right\rangle_{\mathcal{L}^2(\Omega_{2D})} \\ \quad - \left\langle \mathcal{F}_k(\mathbf{F}) \, , \, \mathcal{F}_{k-l}(\boldsymbol{k}_{NEW}^2)\mathcal{F}_l(\mathbf{E}) \right\rangle_{\mathcal{L}^2(\Omega_{2D})} \\ \quad = -j\omega \left\langle \mathcal{F}_k(\mathbf{F}) \, , \, \mathcal{F}_k(\mathbf{J}_{NEW}^{imp}) \right\rangle_{\mathcal{L}^2(\Omega_{2D})} \\ \quad + j\omega \left\langle \mathcal{F}_k(\mathbf{F}_t) \, , \, \mathcal{F}_k(\mathbf{J}_{S,NEW}^{imp}) \right\rangle_{\mathcal{L}^2(\Gamma_H(\Omega_{2D}))} \\ \quad - \left\langle \mathcal{F}_k(\boldsymbol{\nabla}^{\boldsymbol{\zeta}}\times\mathbf{F}) \, , \, \mathcal{F}_{k-l}(\boldsymbol{\mu}_{NEW}^{-1})\mathcal{F}_l(\mathbf{M}_{NEW}^{imp}) \right\rangle_{\mathcal{L}^2(\Omega_{2D})} \\ \quad \forall \, \mathcal{F}_k(\mathbf{F}) \in \mathcal{V}_k(\Omega) \, , \end{cases} \tag{22}$$

where $\Omega_{2D} = \{(\zeta_1, \zeta_2, \zeta_3) \in \Omega : \zeta_2 = 0\}$, and $\mathcal{V}_k(\Omega) = \{\mathcal{F}_k(\mathbf{F})e^{jk\zeta_2} : \mathbf{F} \in V(\Omega)\}$. In the above formula, for each equation k, we are employing Einstein summation convention for $-\infty \leq l \leq \infty$. However, for the problems considered in this paper, if we employ the non-orthogonal coordinate systems described by Equation (1) for deviated wells, we note that $\mathcal{F}_{k-l}(\boldsymbol{\mu}_{NEW}^{-1}) \equiv \mathcal{F}_{k-l}(\boldsymbol{k}_{NEW}^2) \equiv 0$ if $|k-l| > 2$. Therefore, the infinite series in terms of l reduces for each k to a finite sum with at most five terms, namely $l = k-2, ..., k+2$.

2.3 H-Formulation

In this subsection, we derive a formulation of our method in terms of magnetic field $\mathbf{H}$. This derivation follows the same steps as the ones employed for the derivation of the E-Formulation (subsection 2.2).

2.3.1 3D Variational Formulation in Cartesian Coordinates

By dividing Ampere's law by $\boldsymbol{\sigma} + j\omega\boldsymbol{\epsilon}$, pre-multiplying the resulting equation by $\boldsymbol{\nabla}\times\mathbf{F}$, where $\mathbf{F} \in H_{\Gamma_H}(\mathbf{curl};\Omega) = \{\mathbf{F} \in H(\mathbf{curl};\Omega) \ : (\mathbf{n}\times\mathbf{F})|_{\Gamma_H} = 0 \}$ is an arbitrary test function, integrating over the domain $\Omega \subset \mathbb{R}^3$ by parts, and applying Faraday's law, we arrive at the following variational formulation after incorporating the natural and essential boundary conditions over $\Gamma_E \subset \partial\Omega$ and

$\Gamma_H \subset \partial\Omega$, respectively:

$$\begin{cases} \text{Find } \mathbf{H} \in \mathbf{H}_{\Gamma_H} + H_{\Gamma_E}(\mathbf{curl};\Omega) \text{ such that:} \\ \left\langle \boldsymbol{\nabla}\times\mathbf{F}\ ,\ (\boldsymbol{\sigma}+j\omega\boldsymbol{\epsilon})^{-1}\boldsymbol{\nabla}\times\mathbf{H}) \right\rangle_{L^2(\Omega)} + j\omega\left\langle \mathbf{F}\ ,\ \boldsymbol{\mu}\mathbf{H}\right\rangle_{L^2(\Omega)} \\ = -\left\langle \mathbf{F}\ ,\ \mathbf{M}^{imp}\right\rangle_{L^2(\Omega)} + \left\langle \mathbf{F}_t\ ,\ \mathbf{M}_S^{imp}\right\rangle_{L^2(\Gamma_E)} \\ + \left\langle \boldsymbol{\nabla}\times\mathbf{F}\ ,\ (\boldsymbol{\sigma}+j\omega\boldsymbol{\epsilon})^{-1}\mathbf{J}^{imp}\right\rangle_{L^2(\Omega)} \quad \forall\, \mathbf{F} \in H_{\Gamma_H}(\mathbf{curl};\Omega)\ , \end{cases} \tag{23}$$

where $\mathbf{H}_{\Gamma_E}$ is a lift (typically $\mathbf{H}_{\Gamma_H} = 0$) of the essential boundary condition data $\mathbf{H}_{\Gamma_H}$ (denoted by the same symbol), $\mathbf{F}_t = \mathbf{F} - (\mathbf{F}\cdot\mathbf{n})\cdot\mathbf{n}$ is the tangential component of vector $\mathbf{F}$ on Γ_E, and $\mathbf{n}$ is the unit normal outward (with respect to Ω) vector.

2.3.2 3D Variational Formulation in an Arbitrary System of Coordinates

By introducing a possibly non-orthogonal system of coordinates $\boldsymbol{\zeta} = (\zeta_1, \zeta_2, \zeta_3)$, and following an identical derivation as in Section 2.2.2, we arrive at variational formulation (23) with new material coefficients and load data described by Equation (12).

2.3.3 Fourier Series Expansion

To obtain the variational formulation in terms of the Fourier series modal coefficients with respect to variable ζ_2, we follow the derivation performed in Section 2.2.3 to arrive at

$$\begin{cases} \text{Find } \mathcal{F}_k(\mathbf{H}) \in \mathcal{F}_k(\mathbf{H}_{\Gamma_H(\Omega_{2D})}) + \mathcal{V}(\Omega) \text{ such that:} \\ \left\langle \mathcal{F}_k(\boldsymbol{\nabla}^{\boldsymbol{\zeta}}\times\mathbf{F})\ ,\ \mathcal{F}_{k-l}((\boldsymbol{\sigma}_{NEW}+j\omega\boldsymbol{\epsilon}_{NEW})^{-1})\mathcal{F}_l(\boldsymbol{\nabla}^{\boldsymbol{\zeta}}\times\mathbf{H}))\right\rangle_{\mathcal{L}^2(\Omega_{2D})} \\ + j\omega\left\langle \mathcal{F}_k(\mathbf{F})\ ,\ \mathcal{F}_{k-l}(\boldsymbol{\mu}_{NEW})\mathcal{F}_l(\mathbf{H})\right\rangle_{\mathcal{L}^2(\Omega_{2D})} \\ = -\left\langle \mathcal{F}_k(\mathbf{F})\ ,\ \mathcal{F}_k(\mathbf{M}_{NEW}^{imp})\right\rangle_{\mathcal{L}^2(\Omega_{2D})} + \left\langle \mathcal{F}_k(\mathbf{F})\ ,\ \mathcal{F}_k(\mathbf{M}_{S,NEW}^{imp})\right\rangle_{\mathcal{L}^2(\Gamma_E(\Omega_{2D}))} \\ + \left\langle \mathcal{F}_k(\boldsymbol{\nabla}^{\boldsymbol{\zeta}}\times\mathbf{F})\ ,\ \mathcal{F}_{k-l}((\boldsymbol{\sigma}_{NEW}+j\omega\boldsymbol{\epsilon}_{NEW})^{-1})\mathcal{F}_l(\mathbf{J}_{NEW}^{imp})\right\rangle_{\mathcal{L}^2(\Omega_{2D})} \\ \forall\, \mathcal{F}_k(\mathbf{F}) \in \mathcal{V}(\Omega)\ , \end{cases} \tag{24}$$

2.4 Potential Formulations

The described method is also suitable for potential formulations. In this subsection, we outline the main steps necessary to derive a formulation of our method based on vector and/or scalar potentials.

To derive a potential-based formulation stemming from our method, we first consider a suitable system of coordinates for deviated wells, as the one described by Equation (1) and used in subsections 2.2 and 2.3.

Second, we define new materials $\boldsymbol{\sigma}_{NEW}, \boldsymbol{\epsilon}_{NEW}, \boldsymbol{\mu}_{NEW}, \boldsymbol{k}^2_{NEW}$ and impressed volume currents $\mathbf{J}^{imp}_{NEW}, \mathbf{M}^{imp}_{NEW}, \mathbf{J}^{imp}_{S,NEW}, \mathbf{M}^{imp}_{S,NEW}$, as described in Equation (12). These new material tensors and sources incorporate the information about the change of coordinates. As with the case of the E-formulation—subsection 2.2—and with the H-formulation—subsection 2.3—, any potential-based variational formulation can also be expressed in terms of an arbitrary system of coordinates by simply considering the new materials and sources.

Finally, we employ a Fourier series expansion in terms of the periodic quasi-azimuthal variable ζ_2 to derive the potential-based variational formulation in terms of the Fourier modal coefficients.

2.5 Stabilized Variational Formulation

In this subsection, we discuss the advantages of using a stabilized variational formulation that incorporates an unknown scalar potential.

In our derivation of the variational formulations described by Equations (22) and (24), we employed only two Maxwell's equations, namely, Ampere's and Faraday's laws. We note that for a nonzero frequency $\omega \neq 0$, Gauss' laws of electricity and magnetism can be derived from Ampere's and Faraday's laws, and therefore, there is no need to introduce Gauss' laws since they are implicitly satisfied. However, for $\omega = 0$, Ampere and Faraday laws alone provide a non-unique solution, since the divergence of electric and magnetic fields remains undetermined. Specifically, in the case of Formulations (22) and (24), the (ζ_1, ζ_3)-components of the EM fields are undetermined for $\omega = 0$. Thus, Gauss' laws are not automatically satisfied. In summary, solutions of the variational formulations considered in this paper are non-unique when $\omega = 0$.

From the numerical point of view, the non-uniqueness of the solution for $\omega = 0$ implies that the problem becomes numerically unstable as $\omega \to 0$, or equivalently, when element size $h \to 0$ for a fixed frequency.

As a remedy for this problem, we may re-impose explicitly Gauss' laws by introducing a Lagrange multiplier p (which can be interpreted as a scalar potential) as described for example, in [22,26].

For simplicity, in this paper we avoid the use of stabilized variational formulations. However, we emphasize that our method is compatible with the use of a stabilized formulations, and that the corresponding derivations are straightforward.

2.6 A Self-Adaptive Goal-Oriented hp-FE Method

Each of the above Fourier modal coefficients represents a 2D vector-valued function in terms of variables ζ_1 and ζ_3. Furthermore, variational problems (22) and (24) constitute a system of linear equations in terms of 2D functions (Fourier modal coefficients). To solve the above system of linear equations, it is necessary to select a software capable of simulating 2D problems involving coupled $H(\mathbf{curl})$- and H^1-discretizations. The choice of the 2D software is somehow arbitrary, since the Fourier series expansion in terms of the quasi-azimuthal component ζ_2 is independent of the algorithm employed to discretize each 2D problem with respect to variables ζ_1 and ζ_3.

In this work, we have selected as our starting point a 2D self-adaptive goal-oriented *hp*-FE method. This goal-oriented *hp*-FE method delivers exponential convergence rates in terms of the error in the quantity of interest versus the number of unknowns and CPU time; the outstanding performance of the *hp*-FE method for simulating diverse resistivity logging measurements has been documented in [5–7]. A description of the *hp*-FE method can be found in [22]. We refer to [18] for technical details on the goal-oriented adaptive algorithm applied to electrodynamic simulation problems.

3 Implementation

In this Section, we first assume that we have a software capable of solving 2D AC problems with arbitrary material tensors $\boldsymbol{\epsilon}, \boldsymbol{\mu}, \boldsymbol{\sigma}, \boldsymbol{k}^2$ and sources $\mathbf{M}^{imp}, \mathbf{J}^{imp}$. Then, we describe the modifications that are necessary in order to simulate 3D AC borehole measurements acquired in deviated or eccentered wells using the method introduced in Section 2.

First, we define a suitable FE discretization of space $\mathcal{V}(\Omega)$ using mixed 2D *hp*-Finite Elements.

3.1 Finite Element Discretization

We start by analyzing the following space:

$$V(\Omega) = \{\mathbf{F} \ : \ (\mathbf{n}\times\mathbf{F})|_{\Gamma_E} = 0 \, , \ \boldsymbol{\mathcal{J}}^{-1^*}\mathbf{F} \in \boldsymbol{L}^2(\Omega) \, , \ \frac{\boldsymbol{\mathcal{J}}}{|\boldsymbol{\mathcal{J}}|}\boldsymbol{\nabla}^{\boldsymbol{\zeta}}\times\mathbf{F} \in \boldsymbol{L}^2(\Omega)\} \, . \tag{25}$$

The above $H(\mathbf{curl})$-type space exhibits a singularity at $\zeta_1 = 0$ because the change of coordinates is also singular at $\zeta_1 = 0$. While we may employ a standard $H(\mathbf{curl};\Omega)$-FE discretization for elements away from the axis $\zeta_1 = 0$, we should analyze the singularity occurring at $\zeta_1 = 0$ in order to select a proper discretization embedded into $V(\Omega)$. To investigate the conditions required at $\zeta_1 = 0$, we note that

$$\begin{aligned} &|\boldsymbol{\mathcal{J}}^{-1^*}\mathbf{F}|^2 = \mathbf{F}^*\boldsymbol{\mathcal{J}}^{-1}\boldsymbol{\mathcal{J}}^{-1^*}\mathbf{F} = \mathbf{F}^*\boldsymbol{\mathcal{G}}^{-1}\mathbf{F} \, , \text{and} \\ &|\frac{\boldsymbol{\mathcal{J}}}{|\boldsymbol{\mathcal{J}}|}\boldsymbol{\nabla}^{\boldsymbol{\zeta}}\times\mathbf{F}|^2 = (\boldsymbol{\nabla}^{\boldsymbol{\zeta}}\times\mathbf{F})^*\frac{\boldsymbol{\mathcal{J}}^*}{|\boldsymbol{\mathcal{J}}|}\frac{\boldsymbol{\mathcal{J}}}{|\boldsymbol{\mathcal{J}}|}\boldsymbol{\nabla}^{\boldsymbol{\zeta}}\times\mathbf{F} = (\boldsymbol{\nabla}^{\boldsymbol{\zeta}}\times\mathbf{F})^*\frac{\boldsymbol{\mathcal{G}}}{|\boldsymbol{\mathcal{J}}|^2}\boldsymbol{\nabla}^{\boldsymbol{\zeta}}\times\mathbf{F} \, . \end{aligned} \tag{26}$$

Substitution of Equation (26) into Equation (25) provides the following description of space $V(\Omega)$:

$$\begin{aligned} V(\Omega) = \{\mathbf{F} \quad : \quad & (\mathbf{n}\times\mathbf{F})|_{\Gamma_E} = 0 \, , \int_\Omega \mathbf{F}^*\boldsymbol{\mathcal{G}}^{-1}\mathbf{F}|\boldsymbol{\mathcal{J}}| \, d\zeta_1 d\zeta_2 d\zeta_3 < \infty \, , \\ & \int_\Omega (\boldsymbol{\nabla}^{\boldsymbol{\zeta}}\times\mathbf{F})^*\frac{\boldsymbol{\mathcal{G}}}{|\boldsymbol{\mathcal{J}}|^2}(\boldsymbol{\nabla}^{\boldsymbol{\zeta}}\times\mathbf{F})|\boldsymbol{\mathcal{J}}| \, d\zeta_1 d\zeta_2 d\zeta_3 < \infty\}. \end{aligned} \tag{27}$$

For $\zeta_1 < \rho_1$, according to Equation (1) we have

$$\boldsymbol{\mathcal{G}} = \begin{pmatrix} 1 & 0 & 0 \\ 0 & \zeta_1^2 & 0 \\ 0 & 0 & 1 \end{pmatrix} \quad ; \quad \boldsymbol{\mathcal{G}}^{-1} = \begin{pmatrix} 1 & 0 & 0 \\ 0 & \frac{1}{\zeta_1^2} & 0 \\ 0 & 0 & 1 \end{pmatrix} \quad ; \quad |\boldsymbol{\mathcal{J}}| = \zeta_1 \, . \tag{28}$$

Therefore, when $\zeta_1 < \rho_1$, we obtain

$$V(\Omega) = \{\mathbf{F} \;\; : \;\; (\mathbf{n}\times\mathbf{F})|_{\Gamma_E} = 0\,, \int_\Omega \zeta_1|F_{\zeta_1}|^2 + \frac{1}{\zeta_1}|F_{\zeta_2}|^2 + \zeta_1|F_{\zeta_3}|^2 + \frac{1}{\zeta_1}\left|\frac{\partial F_{\zeta_3}}{\partial\zeta_2} - \frac{\partial F_{\zeta_2}}{\partial\zeta_3}\right|^2 + \zeta_1\left|\frac{\partial F_{\zeta_1}}{\partial\zeta_3} - \frac{\partial F_{\zeta_3}}{\partial\zeta_1}\right|^2 + \frac{1}{\zeta_1}\left|\frac{\partial F_{\zeta_2}}{\partial\zeta_1} - \frac{\partial F_{\zeta_1}}{\partial\zeta_2}\right|^2 d\zeta_1 d\zeta_2 d\zeta_3 < \infty\} \tag{29}$$

From the above description of space $V(\Omega)$, it is possible to directly obtain a set of conditions that need to be satisfied at $\zeta_1 = 0$. However we take a different approach. We note that for cylindrical coordinates (ρ, ϕ, z), we have $\mathbf{F} = F_\rho\mathbf{e}_\rho + F_\phi\mathbf{e}_\phi + F_z\mathbf{e}_z$, and $\mathbf{F} = F_{\zeta_1}\mathbf{e}_{\zeta_1} + F_{\zeta_2}\mathbf{e}_{\zeta_2} + F_{\zeta_3}\mathbf{e}_{\zeta_3}$. A simple algebraic exercise shows that:

$$F_\rho = F_{\zeta_1} \quad , \quad F_\phi = \zeta_1 F_{\zeta_2} \quad , \text{ and } \quad F_z = F_{\zeta_3}\,. \tag{30}$$

The above relationships between (F_ρ, F_ϕ, F_z) and $(F_{\zeta_1}, F_{\zeta_2}, F_{\zeta_3})$ indicate that replacing variable F_{ζ_2} with new variable $F_{\zeta_2}^{NEW} := \zeta_1 F_{\zeta_2}$ may be convenient to avoid a singularity at $\zeta_1 = 0$. Thus, we slightly modify our variational formulation and solve for the new unknown $F_{\zeta_2}^{NEW}$. For simplicity, we shall denote the new unknown $F_{\zeta_2}^{NEW}$ simply as F_{ζ_2} (note the abuse of notation). After this change of variable, we have

$$V(\Omega) = \{\mathbf{F} \;\; : \;\; (\mathbf{n}\times\mathbf{F})|_{\Gamma_E} = 0\,, \int_\Omega \zeta_1|F_{\zeta_1}|^2 + \zeta_1|F_{\zeta_2}|^2 + \zeta_1|F_{\zeta_3}|^2 + \frac{1}{\zeta_1}\left|\frac{\partial F_{\zeta_3}}{\partial\zeta_2} - \zeta_1\frac{\partial F_{\zeta_2}}{\partial\zeta_3}\right|^2 + \zeta_1\left|\frac{\partial F_{\zeta_1}}{\partial\zeta_3} - \frac{\partial F_{\zeta_3}}{\partial\zeta_1}\right|^2 + \frac{1}{\zeta_1}\left|\frac{\partial(\zeta_1 F_{\zeta_2})}{\partial\zeta_1} - \frac{\partial F_{\zeta_1}}{\partial\zeta_2}\right|^2 d\zeta_1 d\zeta_2 d\zeta_3 < \infty\}\,. \tag{31}$$

Thus, when discretizing $V(\Omega)$ with $H(\mathbf{curl})$-FE, we need to impose the following conditions at the axis $\zeta_1 = 0$:

$$\frac{\partial F_{\zeta_3}}{\partial\zeta_2} = 0 \quad ; \quad F_{\zeta_2} = \frac{\partial F_{\zeta_1}}{\partial\zeta_2}\,. \tag{32}$$

By expanding $\mathbf{F}$ in terms of a Fourier series with respect to ζ_2, Equation (32) becomes

$$jk\mathcal{F}_k(F_{\zeta_3}) = 0 \quad , \text{ and } \quad \mathcal{F}_k(F_{\zeta_2}) = jk\mathcal{F}_k(F_{\zeta_1}) \quad \forall k\,. \tag{33}$$

From a practical point of view, the above conditions are implemented as boundary conditions, although they should be mathematically (and physically) referred to as *finite energy* conditions or *integrability* conditions, since there is no boundary at $\zeta_1 = 0$ in the original 3D domain. We distinguish between two cases, according to the value of k, namely,

$$\begin{aligned} &k = 0 \ : \mathcal{F}_0(F_{\zeta_2}) = 0 \ , \\ &k \neq 0 \ : \mathcal{F}_k(F_{\zeta_3}) = 0 \quad \text{, and} \quad \mathcal{F}_k(F_{\zeta_2}) = jk\mathcal{F}_k(F_{\zeta_1}) \ . \end{aligned} \tag{34}$$

After expanding $\mathbf{F}$ in terms of Fourier modes with respect to ζ_2, we note that all components of the solution are continuous with respect to ζ_2 because the material coefficients are also continuous with respect to ζ_2. Thus, F_{ζ_2} can be discretized using $H^1(\Omega)$-FE.

Based on the above remarks, our FE space $\mathcal{V}_{hp}$ is defined as

$$\begin{aligned} \mathcal{V}_{hp}^k = \{ &\mathcal{F}_k(\mathbf{F}) \in \mathcal{V}_{hp}^{Hcurl} \times \mathcal{V}_{hp}^{H1} \ : \mathbf{n} \times \mathcal{F}_k(\mathbf{F})|_{\Gamma_E} = 0, \\ &\text{such that the conditions of Equation (34) are satisfied}\}, \end{aligned} \tag{35}$$

where $\mathcal{V}_{hp}^{Hcurl}$ is a FE discretization of space $H(\mathbf{curl};\Omega)$, and $\mathcal{V}_{hp}^{Hcurl}$ is a FE discretization of space $H^1(\Omega)$. Notice that spaces $\mathcal{V}_{hp}^{Hcurl}$ and $\mathcal{V}_{hp}^{H1}$ are independent of k, since we use a unique grid (with different integrability conditions at ζ_1=0) for all Fourier modes. This grid is automatically constructed using a sophisticated self-adaptive goal-oriented *hp*-FE method for electrodynamics (see [18]), where h indicates the element size, and p the polynomial order of approximation within each element.

To summarize, we define as many equations as number of Fourier modal coefficients we want to solve. This number may be modified during execution if the error estimate indicates the necessity of considering additional Fourier modes. We note that each equation contains two unknowns: a 2D vector-valued unknown in the (ζ_1, ζ_3)-direction, and a 2D scalar-valued unknown in the ζ_2-direction. For example, in the case of the E-Formulation, we have $(E_{\zeta_1}, E_{\zeta_3})$, and E_{ζ_2}. The former vector-valued unknown $(E_{\zeta_1}, E_{\zeta_3})$ is discretized with a subspace of $H(\mathbf{curl};\Omega)$, while the latter scalar-valued unknown E_{ζ_2} is discretized with a subspace of $H^1(\Omega)$. Thus, the 2D FE software should enable the simultaneous use of compatible $H(\mathbf{curl};\Omega)-$ and $H^1(\Omega)-$ discretizations. Then, proper boundary conditions and integrability conditions—given by Equation (34)—are imposed.

After selecting a proper FE discretization, we calculate the new material coefficients $\boldsymbol{\epsilon}_{NEW}$, $\boldsymbol{\mu}_{NEW}$, $\boldsymbol{\sigma}_{NEW}$, $\boldsymbol{k}^2_{NEW}$ described in Equation (12). Subsequently, we compute all Fourier modes for the material coefficients, namely,

$\boldsymbol{\epsilon}_{NEW,i}$, $\boldsymbol{\mu}_{NEW,i}$, $\boldsymbol{\sigma}_{NEW,i}$, $\boldsymbol{k}^2_{NEW,i}$, $i=-2,-1,0,1,2$. Additionally, we compute new sources $\mathbf{M}^{imp}_{NEW}$, $\mathbf{J}^{imp}_{NEW}$, $\mathbf{M}^{imp}_{NEW,S}$, $\mathbf{J}^{imp}_{NEW,S}$ and all their Fourier modes $\mathbf{M}^{imp}_{NEW,i}$, $\mathbf{J}^{imp}_{NEW,i}$, $\mathbf{M}^{imp}_{NEW,S,i}$, $\mathbf{J}^{imp}_{NEW,S,i}$, $i=-\infty,...,\infty$. In the following, we assume for simplicity that all sources are volumetric and axisymmetric, that is, $\mathbf{M}^{imp}_{NEW}=\mathbf{M}^{imp}_{NEW,0}$; $\mathbf{J}^{imp}_{NEW}=\mathbf{J}^{imp}_{NEW,0}$; $\mathbf{M}^{imp}_{NEW,S}=\mathbf{0}$; $\mathbf{J}^{imp}_{NEW,S}=\mathbf{0}$.

Next, we need to modify the structure of the stiffness matrix to account for the various equations involved (Fourier modes). Following the ideas used for the DC case (see [1]), we introduce the notation

$$
\begin{aligned}
(k,k-l,l) &:= \left\langle \mathcal{F}_k(\boldsymbol{\nabla}^{\boldsymbol{\zeta}}\times\mathbf{F})\ ,\ \mathcal{F}_{k-l}(\boldsymbol{\mu}^{-1}_{NEW})\ \mathcal{F}_l(\boldsymbol{\nabla}^{\boldsymbol{\zeta}}\times\mathbf{E})\right\rangle_{L^2(\Omega)} \\
&\quad - \left\langle \mathcal{F}_k(\mathbf{F})\ ,\ \mathcal{F}_{k-l}(\boldsymbol{k}^2_{NEW})\mathcal{F}_l(\mathbf{E})\right\rangle_{L^2(\Omega)} \qquad \text{(E-Formulation)} \\
(k,k-l,l) &:= \left\langle \mathcal{F}_k(\boldsymbol{\nabla}^{\boldsymbol{\zeta}}\times\mathbf{F})\ ,\ \mathcal{F}_{k-l}((\boldsymbol{\sigma}_{NEW}+j\omega\boldsymbol{\epsilon}_{NEW})^{-1})\mathcal{F}_l(\boldsymbol{\nabla}^{\boldsymbol{\zeta}}\times\mathbf{H}))\right\rangle_{L^2(\Omega)} \\
&\quad + j\omega\left\langle \mathcal{F}_k(\mathbf{F})\ ,\ \mathcal{F}_{k-l}\boldsymbol{\mu}_{NEW})\mathcal{F}_l(\mathbf{H})\right\rangle_{L^2(\Omega)} \qquad \text{(H-Formulation)}
\end{aligned}
\tag{36}
$$

Then, according to Equations (22) and (24), we obtain the following structure for stiffness matrix A for the specific example of five Fourier modes:

$$
A=\begin{pmatrix}
(-2,0,-2) & (-2,-1,-1) & (-2,-2,0) & 0 & 0 \\
(-1,1,-2) & (-1,0,-1) & (-1,-1,0) & (-1,-2,1) & 0 \\
(0,2,-2) & (0,1,-1) & (0,0,0) & (0,-1,1) & (0,-2,2) \\
0 & (1,2,-1) & (1,1,0) & (1,0,1) & (1,-1,2) \\
0 & 0 & (2,2,0) & (2,1,1) & (2,0,2)
\end{pmatrix}. \tag{37}
$$

In the above matrix, rows and columns are associated with test and trial Fourier modal basis functions, respectively. The resulting stiffness matrix is, in general, penta-diagonal, since the $(k-l)$-th Fourier modal coefficient of the material properties is equal to zero for every $|k-l|>2$.

The resulting system of linear equations needs to be solved with either a direct solver or an iterative solver. An iterative solver requires the implementation of smoothers specially designed to minimize the error of both the rotational and gradient parts of the solution, c.f. [27,28]. For simplicity, and in order to avoid additional numerical errors possibly introduced by the iterative solver, in this paper we use a direct solver. Specifically, we use the parallel multifrontal direct solver MUMPS (version 4.7.3) [29–31], with the ordering of the unknowns provided by METIS (version 4.0) [32]. The interface with the direct solver used in this paper is based on the assembled stiffness matrix format. As emphasized

in [1], to achieve a reasonable performance with our method, it is essential to take advantage of the sparsity of element matrices.

4 Numerical Results

This section is divided into four parts. First, we describe three different models of logging instruments, including two wireline tools operating at 20 Khz and 150 Khz, respectively, and one LWD tool operating at 2 Mhz. At this point, we also describe a model of rock formation consisting of various layers of shales and sands. Second, we present verification results obtained from computations with an uniform formation. Third, we analyze the performance of the software when applied to our model problems of interest. Finally, we perform additional numerical simulations that enable physically consistent conclusions about the three different logging instruments considered in this paper.

4.1 Model Problems

Fig. 2 describes two wireline resistivity logging model instruments. The wireline tool operating at the lowest frequency (20 Khz) exhibits the largest distance between transmitter and first receiver—2 m—, since EM waves in lossy media propagate longer distances at lower frequencies. From the geophysical point of view, measurements acquired with the lowest frequency tool entail the longest radial length of penetration, but the lowest vertical resolution. We note that realistic logging instruments typically incorporate a large number of antennas (8-20) in order to perform several simultaneous measurements, and thus, enhance the radial-vertical focusing of the measurements while minimizing measurement errors. Despite the reduced number of antennas used in our simulations (one transmitter and two receivers), the models of logging instruments considered in this paper have been designed to reproduce the same basic physical principles of those customarily used in actual field operations.

In computer-aided simulations, one may be tempted to model antennas as Dirac's delta functions. However, since the exact solution corresponding to a Dirac's delta load has infinite energy, this load should not be used in combination with self-adaptive codes. Because of this property, we employ finite-size antennas. Specifically, our model loop antennas have a radius of 5 cm and a square cross-section of 2 cm $\times$ 5 cm. Such dimensions are similar to those used in actual logging instruments. Our simulated measurements are given as the

difference of electric field E_ϕ between receivers TX_1 and TX_2, that is,

$$L_1(\mathbf{E}) = \frac{1}{|\Omega_{TX_1}|}\int\limits_{\Omega_{TX_1}} E_\phi dV - \frac{1}{|\Omega_{TX_2}|}\int\limits_{\Omega_{TX_2}} E_\phi dV \ , \tag{38}$$

where $|\Omega_{TX_i}| = \int_{\Omega_{TX_i}} 1dV$. The above quantity of interest is expected to be proportional to the average value (around the receiver antennas) of formation resistivity. The use of two receivers (as opposed to just one) is intended to reduce the effect of primary EM coupling between transmitter and receiver antennas, thereby emphasizing EM signals due to secondary electrical currents induced in the adjacent rock formation.

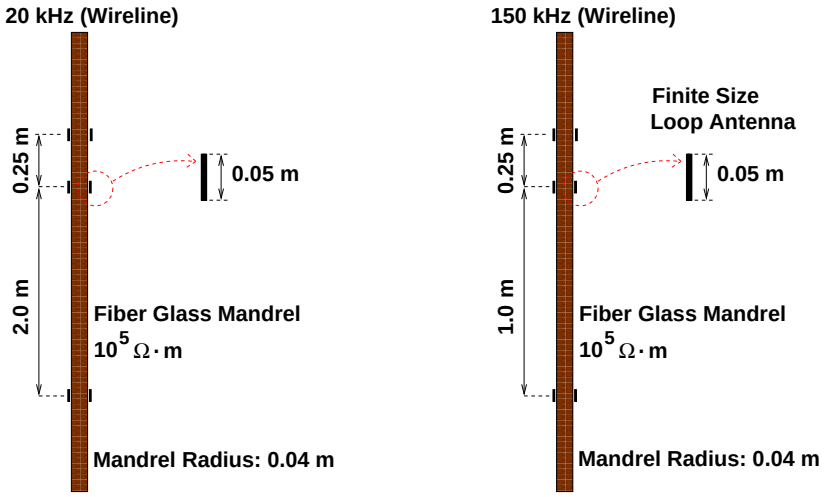

Fig. 2. Two wireline resistivity logging instruments, operating at 20 Khz (left panel) and 150 Khz (right panel), respectively. Each logging instrument is equipped with one transmitter and two receiver loop antennas.

Fig. 3 describes the assumed LWD instrument operating at 2 Mhz. While wireline tools are constructed with a highly resistive (fiber glass) mandrel, LWD instruments are constructed with a highly conductive (metallic) mandrel and incorporate magnetic buffers. The buffers are used to reduce the inductive coupling between antennas and the mandrel, and hence maximize the output impedance of the antennas. We also note that while wireline instrument antennas consist of cable wrapped within the mandrel, in LWD tools the mandrel is indented (as shown in Fig. 3) such that the antennas are embedded within the mandrel, thereby minimizing mechanical friction due to drilling. From a numerical point of view, modeling of the indented mandrel generates strong singularities on the EM fields, which may pollute the solution if not properly accounted for.

The three logging instruments described above are used to acquire measurements in the synthetic reservoir model described in Fig. 4. The formation is

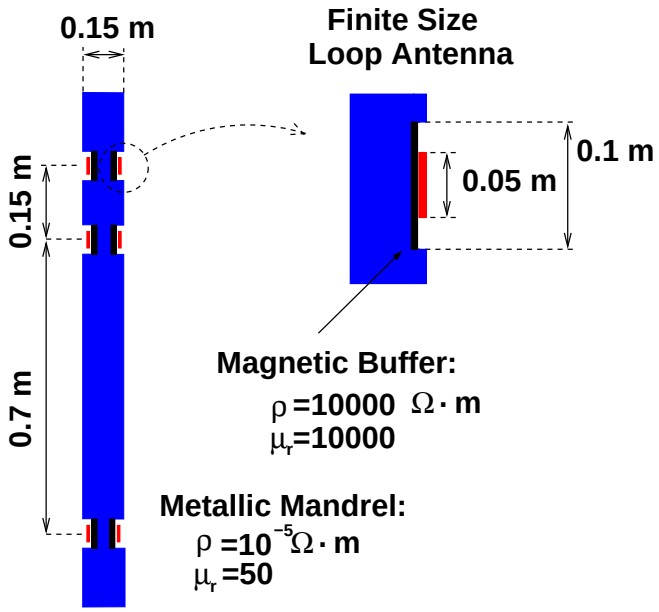

Fig. 3. LWD instrument equipped with one transmitter and two receiver loop antennas operating at 2 Mhz. The mandrel is highly conductive, and antennas are equipped with magnetic buffers.

composed of seven different layers with varying resistivities, from 0.01 Ω· m to 100 Ω· m. We consider a highly resistive oil-based mud in a possibly deviated well. We also include the effect of mud-filtrate radial invasion occurring in three different porous and permeable sand layers.

4.2 Verification of Results and Convergence

This subsection is intended to verify our implementation of the described method. We first observe that in a homogeneous, isotropic and unbounded formation all measurements should coincide independently of dip angle. In particular, regardless of dip angle, the exact solution should coincide with that obtained for the axisymmetric case (vertical well). However, in the case of a deviated well we may need an infinite number of Fourier modes to reproduce the exact solution.

To verify the accuracy and reliability of our code, we first compute a high-accuracy approximation (below 0.01% relative error in the quantity of interest) of the exact solution for a vertical well. This high-accuracy solution is computed with a 2D *hp*-FE code, which has been extensively verified against different numerical methods [18,5,6] and analytical solutions [33]. Using this high-accuracy 2D solution as our exact solution, we study the convergence of our method based on the relative error in the quantity of interest with respect

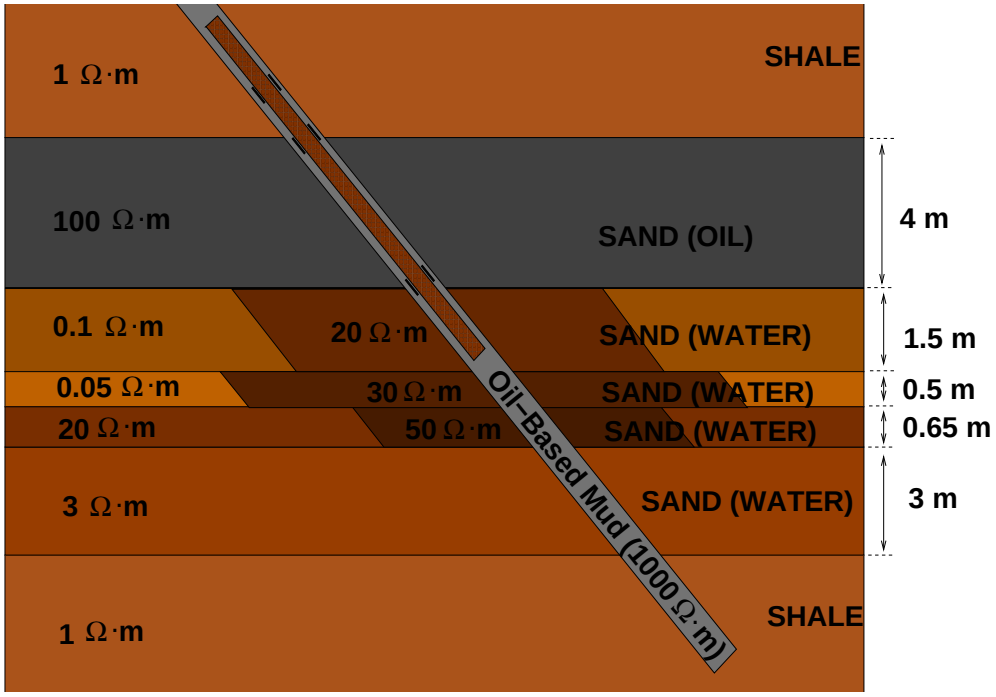

Fig. 4. Deviated well penetrating a reservoir with various water- and oil-bearing sand layers.

to the number of Fourier modes for various dip angles.

We consider an uniform formation of resistivity equal to 1 Ω· m. Convergence histories with respect to the number of Fourier modes for a 30- and a 60-degree deviated wells are displayed in Fig. 5. The three panels of Fig. 5 correspond to the three logging instruments described above. For wireline instruments (top panels) we observe a rapid convergence. With only five Fourier modes, the corresponding error in the quantity of interest drops below 1%. For LWD (bottom panel), fifteen Fourier modes are necessary in order to reduce the relative error in the quantity of interest below 3% for a 60-degree deviated well. As we shall see in the next subsections, a solution with a relative error below 10% is considered a highly accurate solution for all practical purposes.

4.3 Performance and Error Analysis

In this subsection, we consider the wireline logging instrument operating at 150 Khz in conjunction with the model formation shown in Fig. 4 and study the convergence properties of the numerical solution as a function of the number of Fourier modes used in the calculations.

For a fixed number of Fourier modes in the quasi-azimuthal direction, the *hp*-FE strategy automatically generates an optimal grid that delivers an error in

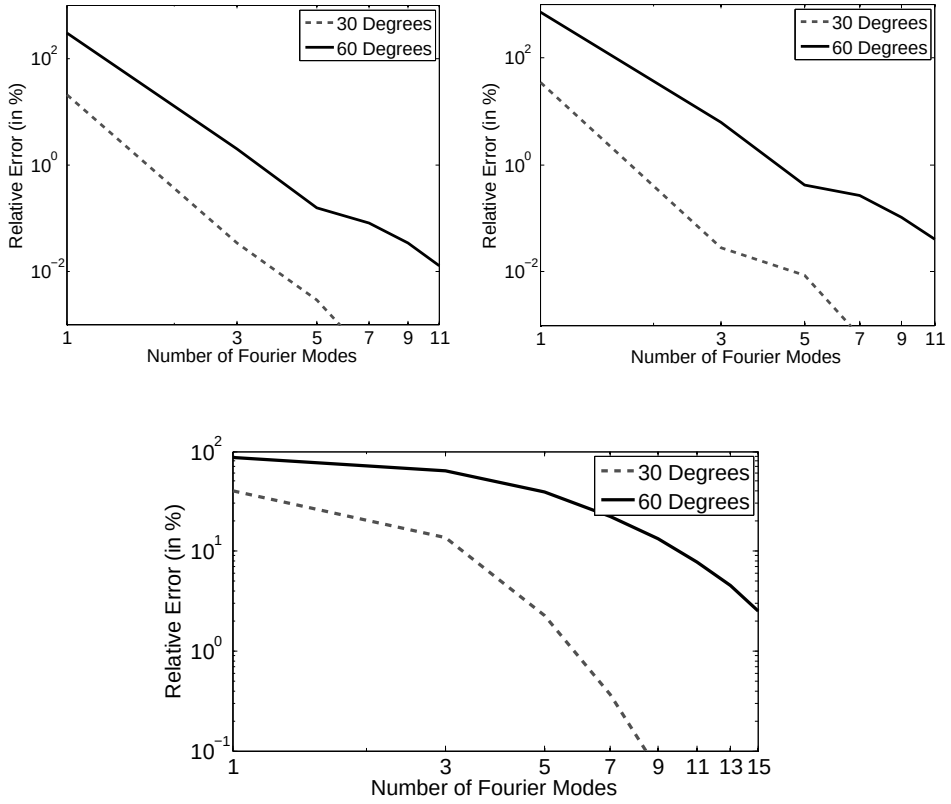

Fig. 5. Convergence history. Relative error vs. number of Fourier modes in a log-log scale. Top panel: Wireline logging instruments operating at 20 Khz (left), and 150 Khz (right), respectively. Bottom panel: LWD instrument operating at 2 Mhz.

the quantity of interest below a given tolerance error. In our case, we select a tolerance error equal to 1%. However, the total error may be considerably larger, since the number of Fourier modes is fixed. Fig. 6 displays the final results (as we move the logging instrument along the well trajectory) for 1, 3, 5, 7, and 9 Fourier modes. When using 3 Fourier modes, the total error is below 5% (see Fig. 6, bottom-right panel), which indicates that the solution is highly accurate for our purposes. As a matter of fact, it is (almost) impossible to observe a difference between the results obtained with 3, 5, 7, or 9 Fourier modes (see Fig. 6, top panels).

Fig. 9 describes similar results for a 60-degree deviated well. As we increase the dip angle, we need to employ a larger number of Fourier modes to achieve a similar level of accuracy. Specifically, we need to consider 7 Fourier modes to guarantee an error below 10% at all logging points. We also find a correlation between the relative error and the electrical conductivity of the formation: in this example, as we increase the electrical conductivity of the formation, we need to utilize more Fourier modes to achieve a similar level of accuracy.

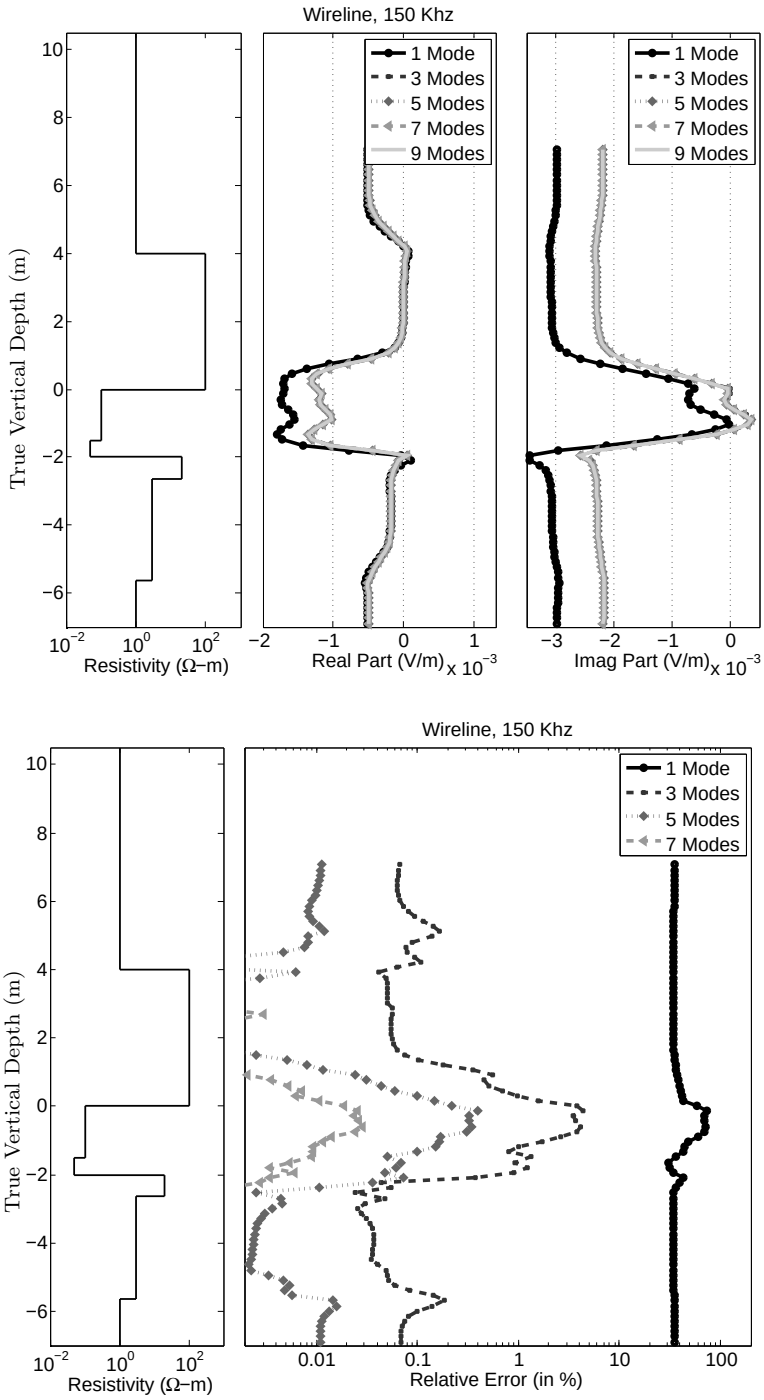

Fig. 6. Wireline instrument operating at 150 Khz in a 30-degree deviated well. Left panels: Formation resistivity. Center-top and right-top panels: Real and imaginary parts of the quantity of interest. Right-bottom panel: Relative error in percentage. Different curves correspond to different numbers of Fourier modes used to calculate the solution.

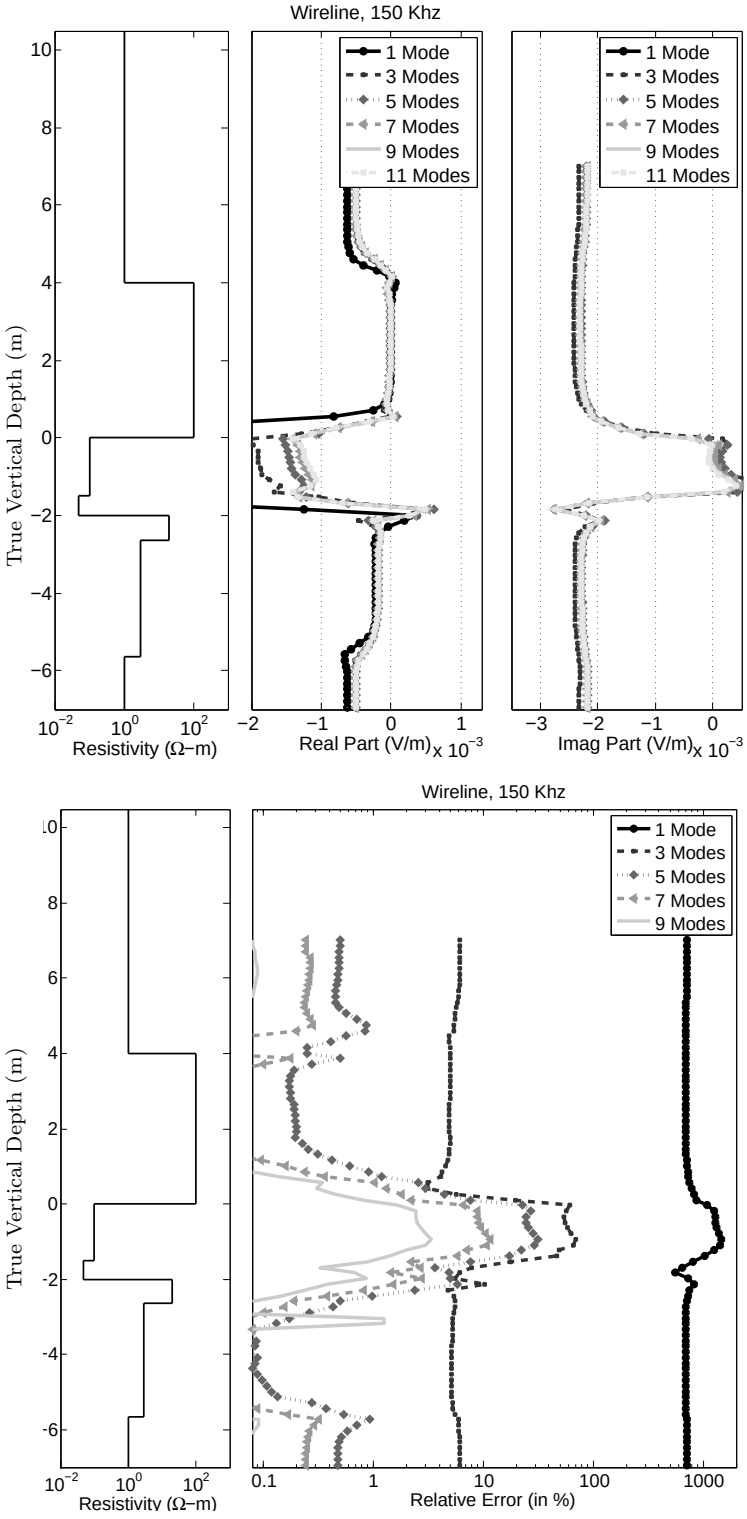

Fig. 7. Wireline instrument operating at 150 Khz in a 60-degree deviated well. Left panels: Formation resistivity. Center-top and right-top panels: Real and imaginary parts of the quantity of interest. Right-bottom panel: Relative error in percentage. Different curves correspond to different numbers of Fourier modes used to calculate the solution.

We note that the CPU time and memory required to construct optimal *hp*-grids using a large number of Fourier modes may become prohibitive. In other words, executing the adaptive algorithm with many Fourier modes is computationally expensive. Thus, we shall restrict ourselves to calculations performed with a limited number of Fourier modes for the construction of adapted *hp*-grids. Subsequently, we shall compute the final solution with a larger number of Fourier modes. Specifically, and following [1], we consider the eight different cases or algorithmic formulations described in Table 1 to perform the simulations. For the *hp* self-adaptive goal-oriented refinement strategy, we select a tolerance error of 1% in the quantity of interest. That is, we enforce that the difference in the quantity of interest corresponding to the solutions in the final coarse and fine (globally *hp*-refined) grids, respectively, remain below 1%. However, the final *hp*-grid may not be optimal due to the fact that we employ a low number of Fourier modes for its construction. Therefore, we shall consider the case of possibly *p*-enriching the final *hp*-grid for increased accuracy (algorithms 2,4,6, and 8).

Case Number **(Algorithmic Implementation)**	**1**	**2**	**3**	**4**	**5**	**6**	**7**	**8**
1 Fourier mode used for adaptivity	X	X	X	X				
5 Fourier modes used for adaptivity					X	X	X	X
Final *hp*-grid NOT *p*-enriched	X		X		X		X	
Final *hp*-grid globally *p*-enriched		X		X		X		X
9 Fourier modes used for the final solution	X	X			X	X		
15 Fourier modes used for the final solution			X	X			X	X

Table 1
Definition of eight different algorithms used for the simulation of borehole resistivity measurements.

In Fig. 8 we display the real part of the solution (top panel) and the relative error (bottom panel) for the wireline instrument operating at 150Khz in a 30-degree deviated well through our model formation. Different curves correspond to simulation results obtained with the eight different algorithms described in Table 1. Relative errors are computed using the solution with 11 Fourier modes (for both adaptivity and solution itself) as the exact solution. Fig. 9 displays the corresponding simulation results for a 60-degree deviated well.

For the 30-degree deviated well, all simulation algorithms provide a relative error below 3% for all logging points. For the 60-degree deviated well, algorithms 1 and 3 provide an error as large as 55%, algorithms 5 through 8 provide an error below 3%, and algorithms 3 and 4 provide an error below 10%. Notice that a relative error below 10% is considered to be small, and the corresponding solution is sufficiently accurate for all practical purposes since,

as shown in Fig. 9, differences on the solutions are hardly noticeable.

As we increase the number of Fourier modes, we also increase the CPU time and memory requirements. Table 2 displays the CPU time used in conjunction with each of the eight algorithms described above. Timings were measured by running the parallel version of the code with eight processors, each of them equipped with 8 GB of RAM memory (see 'Lonestar' machine, [34]). Results indicate that the solution for a 30-degree deviated well can be accurately computed with algorithm 1, which requires only 17 minutes of CPU time for 100 logging positions, that is, an average of 10 seconds per logging position. In order to obtain an accurate solution for a 60-degree deviated well, we need to use algorithms 2 or 4 (10% relative error), or 5 through 8 (below 3% error). Algorithm 4 provides a good compromise between CPU time and accuracy. In this case, we need a total of 84 minutes of CPU time to compute the full solution that includes 100 logging points, that is, below 1 minute per logging position. For a more accurate solution, algorithm 8 requires 4-5 minutes per logging position.

Algorithmic Implementation	**1**	**2**	**3**	**4**	**5**	**6**	**7**	**8**
CPU Time (Minutes) 30-Degree Deviated	17'	49'	36'	131'	144'	188'	173'	269'
CPU Time (Minutes) 60-Degree Deviated	12'	31'	22'	84'	263'	381'	312'	442'

Table 2
CPU simulation time required for the simulation of 100 logging positions as a function of the algorithm (case number) for the wireline instrument operating at 150 Khz in the model formation shown in Fig. 4. The two rows of results correspond to 30- and 60-degree deviated wells, respectively.

4.4 Numerical Applications

In this subsection, we consider the three logging instruments described above and the model formation shown in Fig. 4, and compare results obtained with 0-, 30-, 45-, and 60-degree deviated wells. We also analyze the effect of mud invasion on the simulated measurements.

Fig. 10 displays the real and imaginary parts of the quantity of interest as a function of the vertical position of the receiver antennas for the wireline instrument operating at 20 Khz. Results are displayed in true vertical depth (TVD). As we increase the dip angle, we observe more significant shoulder-bed effects. Specifically, in the bottom part of the most electrically conductive layer, we observe peaks on the simulated measurements for highly deviated wells. This

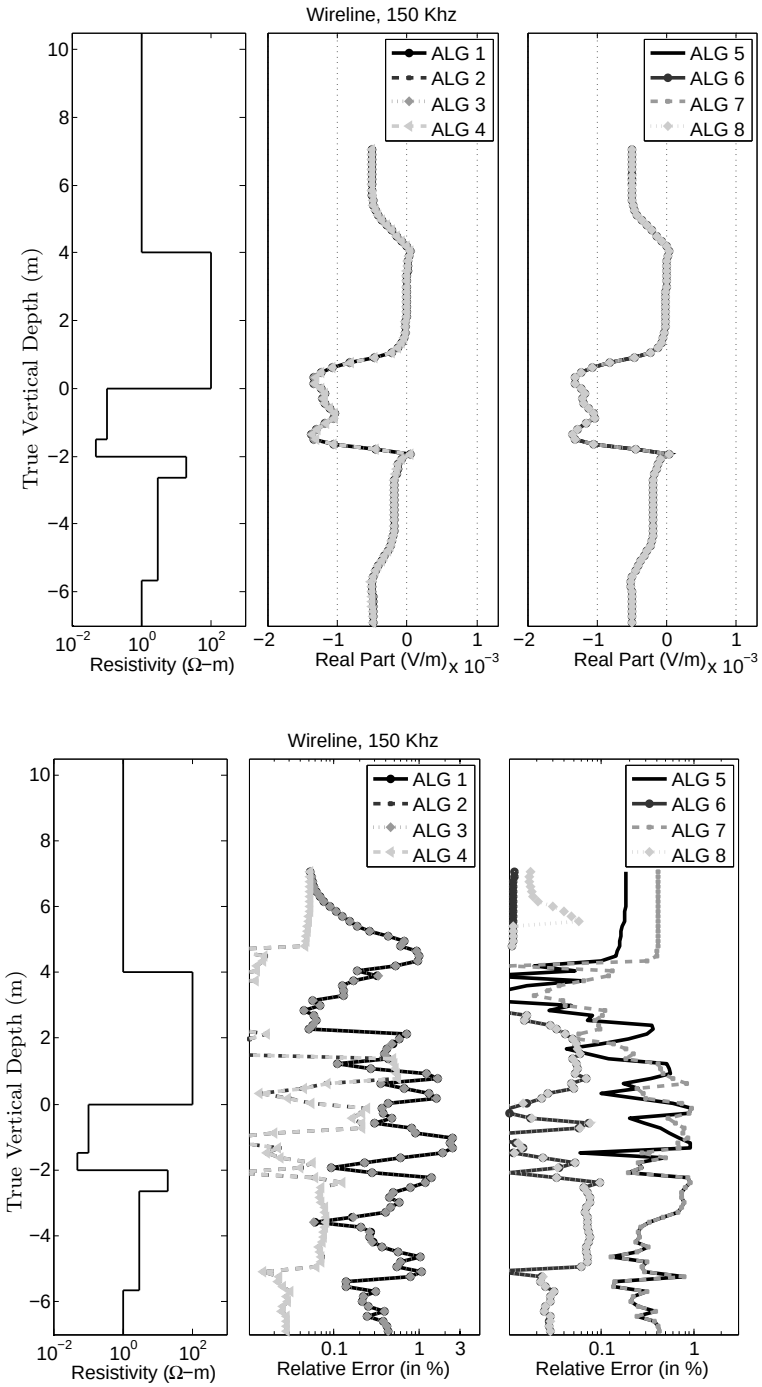

Fig. 8. Wireline instrument operating at 150 Khz in a 30-degree deviated well. Different curves correspond to different algorithms. Top panel: Real part of the solution as a function of the true vertical position of the receivers. Bottom panel: Relative error of the solution as a function of the true vertical position of the receivers.

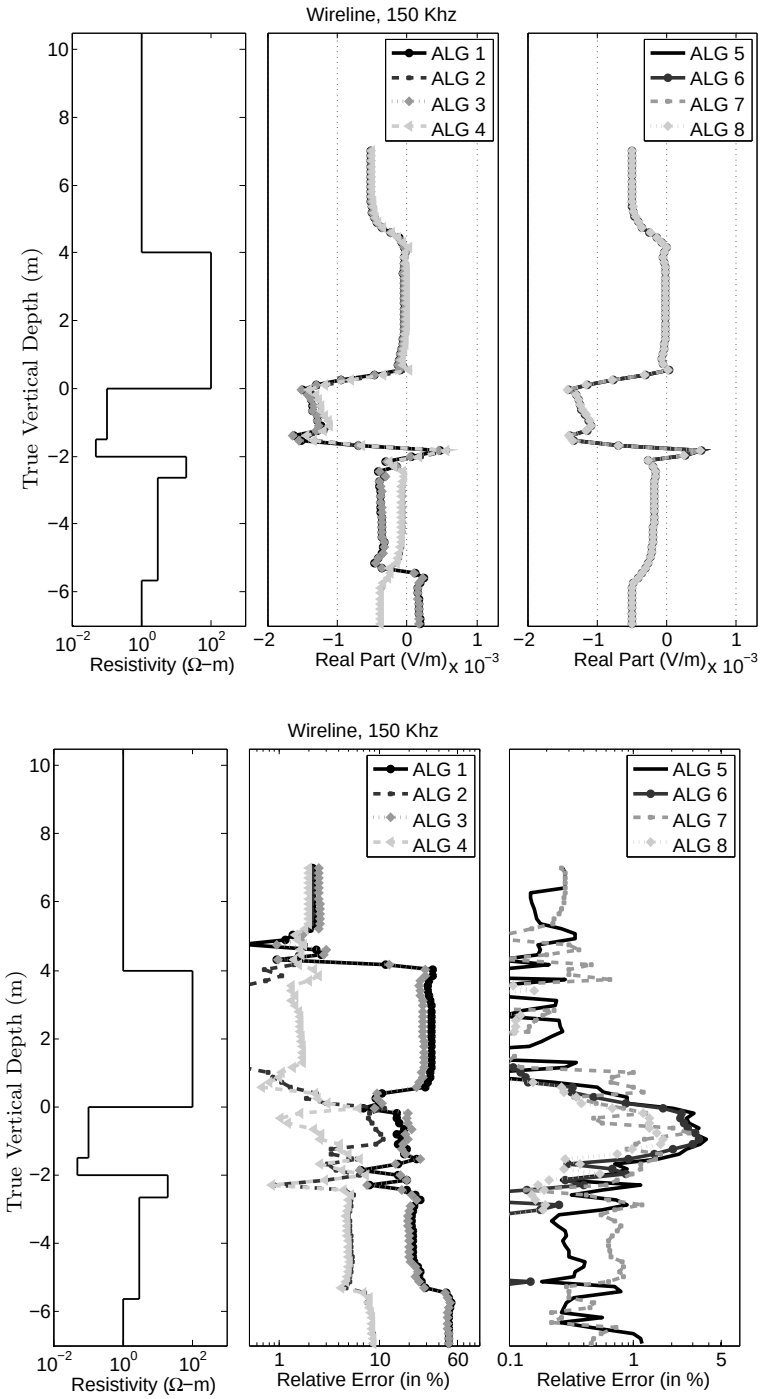

Fig. 9. Wireline instrument operating at 150 Khz in a 60-degree deviated well. Different curves correspond to different algorithms. Top panel: Real part of the solution as a function of the true vertical position of the receivers. Bottom panel: Relative error of the solution as a function of the true vertical position of the receivers.

behavior has been documented in, for example, [12,9]. The thickness of the most conductive layer is better assessed with the results obtained from highly deviated wells. Simulated measurements are also sensitive to the effect of invasion, which can be clearly appreciated by observing the magnitude of the imaginary part of the solution.

Fig. 11 described the corresponding results for the wireline instrument operating at 150 Khz. Shoulder-bed effects at 150 Khz are similar to those observed at 20 Khz. As we increase the frequency of operation, the effect of mud invasion becomes more noticeable. This results are physically consistent, since the radial length of investigation is shorter for high frequencies, whereby measurements are more sensitive to invasion effects.

Finally, in Fig. 12, we display the simulated measurements for the LWD instrument operating at 2 Mhz. We observe a stronger effect of mud invasion than for the case of wireline logging instruments because the frequency of operation is higher for LWD. Also, as we increase the dip angle, we observe more significant shoulder bed effects, mainly at the top of the most electrically conductive layer. As expected, the thickness of the most electrically conductive layer is better assessed with the results obtained for the most highly deviated well. We also observe more pronounced peaks at the shoulders as we increase the dip angle.

5 Conclusions

We have introduced and successfully tested a new simulation method for EM problems based on the use of a non-orthogonal system of coordinates with a Fourier series expansion in one direction. The method is suitable for the simulation of borehole resistivity logging measurements acquired in deviated wells with electrical anisotropy of permeable rock formations. For these geometries, material coefficients are constant in the new system of coordinates, and only five Fourier modes are necessary to reproduce exactly the new materials constructed after incorporating the change of coordinates. The new method is suitable for solving both forward and inverse EM problems.

An elegant derivation of the new variational formulation has been obtained using the unit vectors of the Cartesian system of coordinates with the variables of the new (non-orthogonal) system of coordinates.

Our implementation of the new method of solution is based on the superposition of 2D and 1D algorithms. Thus, the implementation requires a fraction of the time needed to develop a conventional 3D simulator. Also, the CPU time spent by the new solution method is considerably smaller than the CPU time

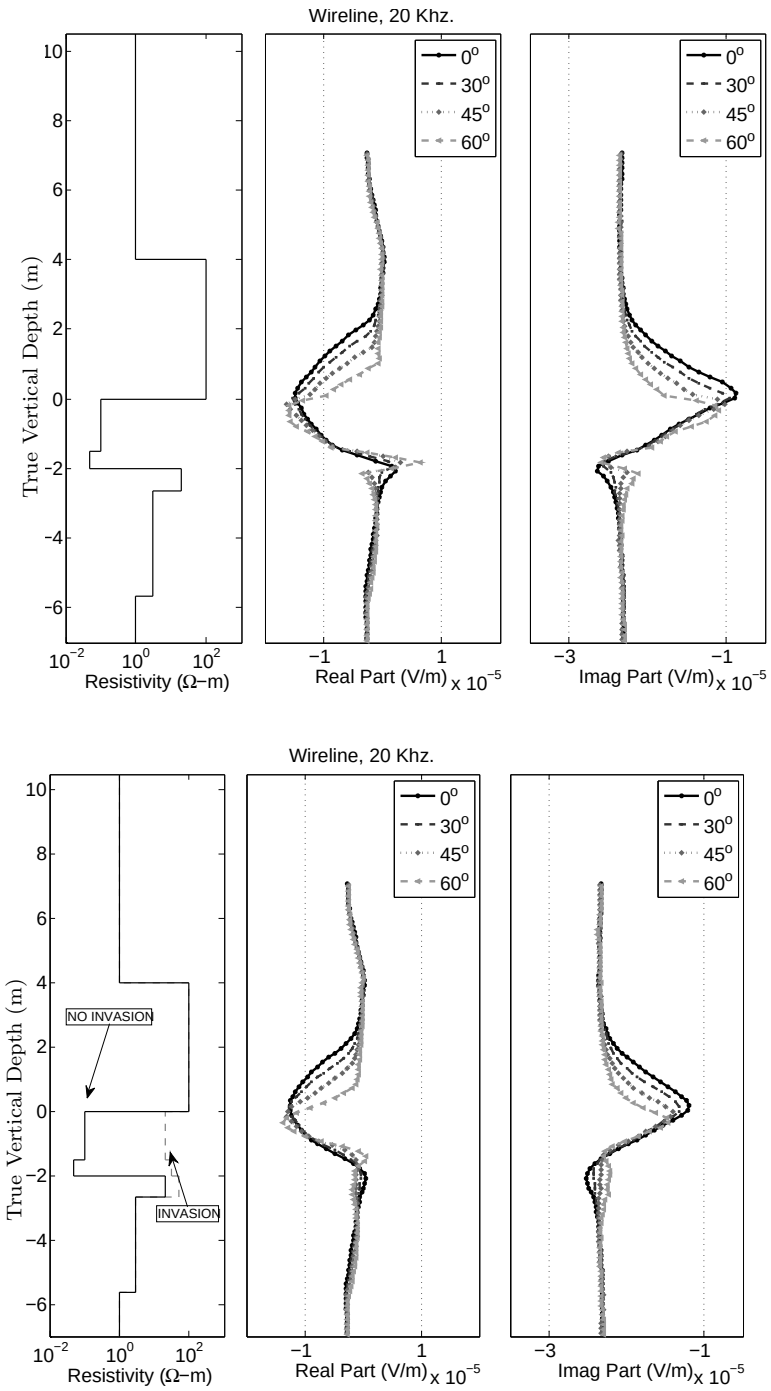

Fig. 10. Quantity of interest as a function of the true vertical position of the receivers for a wireline instrument operating at 20 Khz in a formation without (top panel) and with (bottom panel) invasion. Different curves correspond to different dip angles: 0, 30, 45 and 60 degrees, respectively.

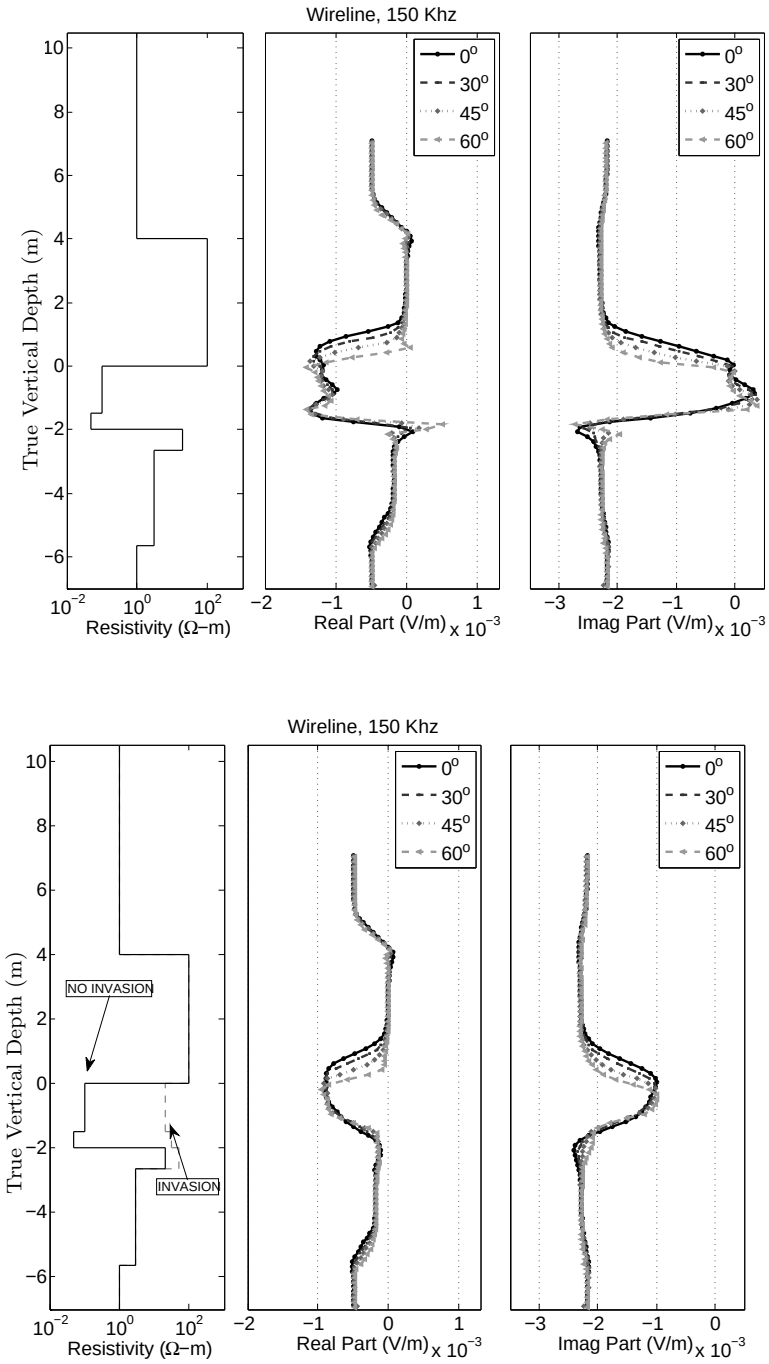

Fig. 11. Quantity of interest as a function of the true vertical position of the receivers for a wireline instrument operating at 150 Khz in a formation without (top panel) and with (bottom panel) invasion. Different curves correspond to different dip angles: 0, 30, 45 and 60 degrees, respectively.

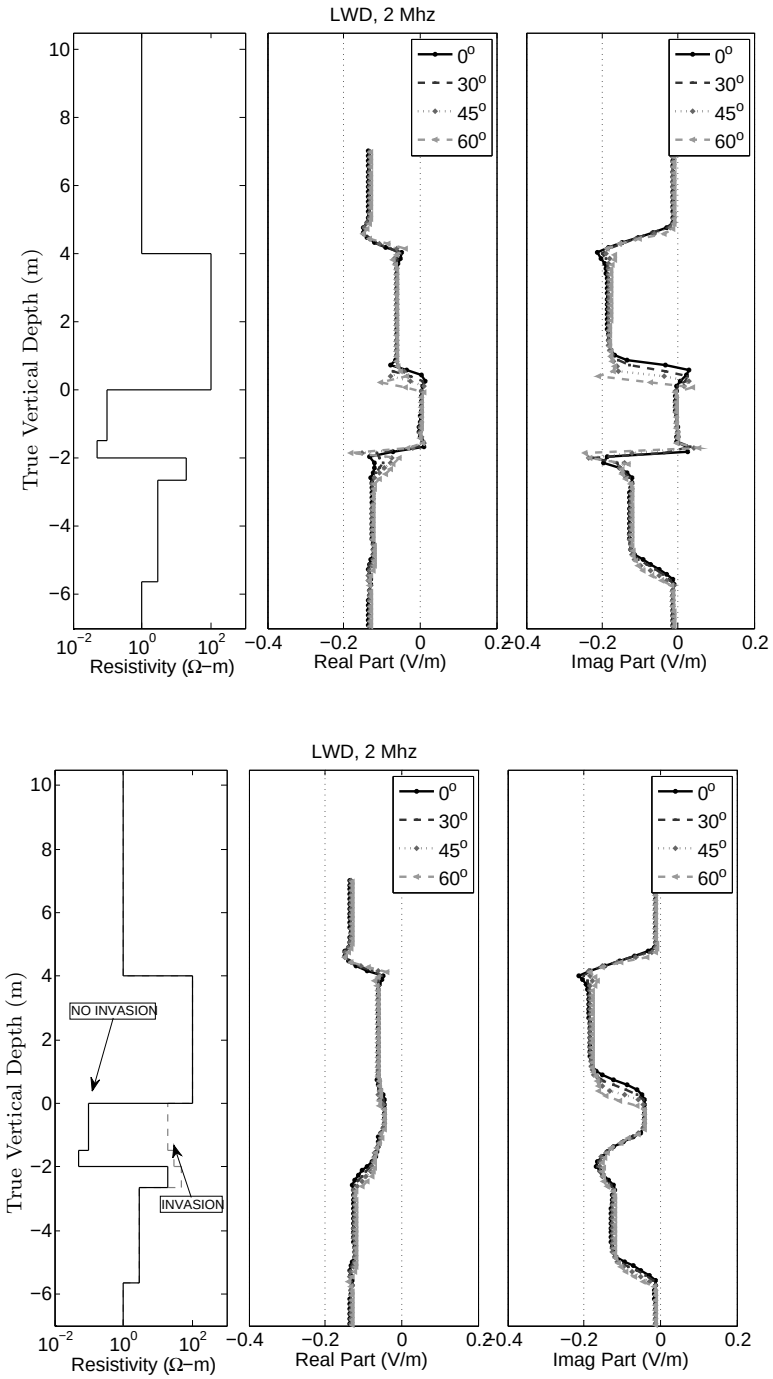

Fig. 12. Quantity of interest as a function of the true vertical position of the receivers for a LWD instrument operating at 2 Mhz in a formation without (top panel) and with (bottom panel) invasion. Different curves correspond to different dip angles: 0, 30, 45 and 60 degrees, respectively.

required by conventional 3D simulators. In order to further reduce the CPU time to a few seconds (or minutes, depending upon the required accuracy) per logging position, we have developed a parallel version of the code. Future work will involve the development of efficient iterative solvers.

We have validated the method, and illustrated its reliability and efficiency. Results indicate that accurate solutions are obtained using only a limited number of Fourier modes for the solution (typically, fewer than 7 for 30-degree deviated wells, and fewer than 13 for 60-degree deviated wells), thereby enabling a significant reduction of computer complexity.

From the physical point of view, simulated measurements indicate a higher sensitive to mud-filtrate invasion in electrical conductive layers. In addition, we observe significant shoulder-bed effects on highly deviated wells. Thus, the new method provides precise quantitative results, and enable the computer-aided study of common effects occurring within the logging industry such as the invasion of mud into permeable formations.

ACKNOWLEDGMENTS

The work presented in this paper was supported by The University of Texas at Austin's *Joint Industry Research Consortium on Formation Evaluation* sponsored by Anadarko, Aramco, Baker Atlas, British Gas, BHP-Billiton, BP, Chevron, Conoco-Phillips, ENI E&P, ExxonMobil, Halliburton, Marathon, Mexican Institute for Petroleum, Hydro, Occidental Petroleum, Petrobras, Schlumberger, Shell E&P, Statoil, TOTAL, and Weatherford International, Ltd. The authors acknowledge the Texas Advanced Computing Center (TACC) at The University of Texas at Austin for providing high performance computing resources that have contributed to the research results reported in this paper.

References

[1] D. Pardo, V. M. Calo, C. Torres-Verdin, M. J. Nam, Fourier series expansion in a non-orthogonal system of coordinates for simulation of 3D DC borehole resistivity measurements, *Accepted* at: Computer Methods in Applied Mechanics and Engineering. Preprint available at: www.ices.utexas.edu/%7Epardo.

[2] B. Heinrich, The fourier-finite-element method for Poisson's equation in axisymmetric domains with edges, SIAM Journal on Numerical Analysis 33 (5) (1996) 1885–1911.

[3] C. Bernardi, M. Dauge, Y. Maday, Spectral Methods for Axisymmetric Domains, ELSEVIER, 1999.

[4] X. Lu, D. L. Alumbaugh, One-dimensional inversion of three-component induction logging in anisotropic media, SEG Expanded Abstract 20 (2001) 376–380.

[5] D. Pardo, L. Demkowicz, C. Torres-Verdin, M. Paszynski, Simulation of resistivity logging-while-drilling (LWD) measurements using a self-adaptive goal-oriented *hp*-finite element method, SIAM Journal on Applied Mathematics 66 (2006) 2085–2106.

[6] D. Pardo, C. Torres-Verdin, L. Demkowicz, Simulation of multi-frequency borehole resistivity measurements through metal casing using a goal-oriented *hp*-finite element method, IEEE Transactions on Geosciences and Remote Sensing 44 (2006) 2125–2135.

[7] D. Pardo, C. Torres-Verdin, L. Demkowicz, Feasibility study for two-dimensional frequency dependent electromagnetic sensing through casing, Geophysics 72 (2007) F111–F118.

[8] J. Zhang, R. L. Mackie, T. R. Madden, 3-D resistivity forward modeling and inversion using conjugate gradients, Geophysics 60 (1995) 1312–1325.

[9] V. L. Druskin, L. A. Knizhnerman, P. Lee, New spectral Lanczos decomposition method for induction modeling in arbitrary 3-D geometry, Geophysics 64 (3) (1999) 701–706.

[10] G. A. Newman, D. L. Alumbaugh, Three-dimensional induction logging problems, part 2: A finite-difference solution, Geophysics 67 (2) (2002) 484–491.

[11] S. Davydycheva, V. Druskin, T. Habashy, An efficient finite-difference scheme for electromagnetic logging in 3D anisotropic inhomogeneous media, Geophysics 68 (5) (2003) 1525–1536.

[12] T. Wang, S. Fang, 3-D electromagnetic anisotropy modeling using finite differences, Geophysics 66 (5) (2001) 1386–1398.

[13] T. Wang, J. Signorelli, Finite-difference modeling of electromagnetic tool response for logging while drilling, Geophysics 69 (1) (2004) 152–160.

[14] D. B. Avdeev, A. V. Kuvshinov, O. V. Pankratov, G. A. Newman, Three-dimensional induction logging problems, part 1: An integral equation solution and model comparisons, Geophysics 67 (2002) 413–426.

[15] D. Pardo, M. Paszynski, C. Torres-Verdin, L. Demkowicz, Simulation of 3D DC borehole resistivity measurements with a goal-oriented *hp* finite element method. Part I: Laterolog and LWD instruments, *Submitted to*: IEEE Geoscience and Remote Sensing Letters. Preprint available at: www.ices.utexas.edu/%7Epardo.

[16] D. Pardo, C. Torres-Verdin, M. Paszynski, Simulation of 3D DC borehole resistivity measurements with a goal-oriented *hp* finite element method. Part II: Through casing resistivity instruments, Computational Geosciences, *in press*. Preprint available at: www.ices.utexas.edu/%7Epardo.

[17] R. F. Harrington, Time-Harmonic Electromagnetic Fields, McGraw-Hill, New York, 1961.

[18] D. Pardo, L. Demkowicz, C. Torres-Verdin, M. Paszynski, A goal oriented hp-adaptive finite element strategy with electromagnetic applications. Part II: electrodynamics, Computer Methods in Applied Mechanics and Engineering. 196 (2007) 3585–3597.

[19] W. Cecot, W. Rachowicz, L. Demkowicz, An *hp*-adaptive finite element method for electromagnetics. III: A three-dimensional infinite element for Maxwell's equations, International Journal of Numerical Methods in Engineering 57 (7) (2003) 899–921.

[20] D. Pardo, L. Demkowicz, C. Torres-Verdin, C. Michler, PML enhanced with a self-adaptive goal-oriented hp finite-element method and applications to through-casing borehole resistivity measurements, *Submitted* to: SIAM Journal on Scientific Computing. Preprint available at: www.ices.utexas.edu/%7Epardo.

[21] I. Gomez-Revuelto, L. E. Garcia-Castillo, D. Pardo, L. Demkowicz, A two-dimensional self-adaptive *hp* finite element method for the analysis of open region problems in electromagnetics, IEEE Transactions on Magnetics 43 (4) (2007) 1337–1340.

[22] L. Demkowicz, Computing with hp-Adaptive Finite Elements. Volume I: One and Two Dimensional Elliptic and Maxwell Problems, Chapman and Hall, 2006.

[23] A. Ward, J. B. Pendry, Calculating photonic Green's functions using a nonorthogonal finite-difference time-domain method, Phys. Rev. B 58 (1998) 7252–9.

[24] W. C. Chew, W. H. Weedon, A 3D perfectly matched medium from modified Maxwell's equations with streched coordinates, Microwave Opt. Tech. Lett. 7 (1994) 599–604.

[25] F. L. Teixeira, W. C. Chew, PML-FDTD in cylindrical and spherical grid, IEEE Microwave Guided Wave Lett. 7 (1997) 285–287.

[26] L. Demkowicz, Finite element methods for Maxwell equations, Encyclopedia of Computational Mechanics, (eds. E. Stein, R. de Borst, T.J.R. Hughes), Wiley and Sons 1 (26).

[27] D. N. Arnold, R. S. Falk, R. Winther, Multigrid in H(div) and H(curl), Numer. Math. 85 (2) (2000) 197–217.

[28] R. Hiptmair, Multigrid method for Maxwell's equations, SIAM J. Numer. Anal. 36 (1) (1998) 204–225.

[29] P. R. Amestoy, I. S. Duff, J.-Y. L'Excellent, Multifrontal parallel distributed symmetric and unsymmetric solvers, Computer Methods in Applied Mechanics and Engineering 184 (2000) 501–520.

[30] P. R. Amestoy, I. S. Duff, J. Koster, J.-Y. L'Excellent, A fully asynchronous multifrontal solver using distributed dynamic scheduling, SIAM Journal of Matrix Analysis and Applications 23 (1) (2001) 15–41.

[31] P. R. Amestoy, A. Guermouche, J.-Y. L'Excellent, S. Pralet, Hybrid scheduling for the parallel solution of linear systems, Parallel Computing 32 (2006) 136–156.

[32] www-users.cs.umn.edu/ karypis/metis, METIS - Family of Multilevel Partitioning Algorithms (2007).

[33] M. Paszynski, L. Demkowicz, D. Pardo, Verification of goal-oriented *hp*-adaptivity, Computers and Mathematics with Applications 50 (2005) 1395–1404.

[34] http://www.tacc.utexas.edu, TACC - Texas Advanced Computing Center (2007).